

# **Ground Truthing Earth's Silicate Weathering Thermostat: Using the Geochemistry of Himalayan Groundwaters to Calculate Residence Times**

Giovanni Bernardi

Part III Project

2024-2025



# **Abstract**

Silicate weathering removes carbon in the form of atmospheric CO<sub>2</sub> and is proposed to be the central control on climate over multi-million year timescales, keeping Earth habitable. The Himalayas are a key region where silicate weathering occurs, and their tectonic uplift has been suggested as a major cause of cooling over the last 40 million years. However, the controls on silicate weathering in real world catchments are not well understood. Temperature has historically been considered the main control on weathering, but recent studies have suggested that water discharge may be more important. Groundwater residence times are important as they can inform recharge from rainwater and the extent of reaction. This study presents a novel approach, using spring and rain water major element concentrations from the Melamchi catchment in Nepal to test these opposing hypotheses by calculating residence times of groundwaters using reactive transport models. Previous studies using gas tracers have estimated residence times in Melamchi to be of the order of 10 years. Results from both model hypotheses agree with the gas ages within error, which given their different assumptions about rate of reaction suggests the sampled springs are far from equilibrium. Free energy of reaction calculations agree. This is inconsistent with the model with assumptions based on a hydrological control of weathering, which this study concludes should not be used for rapidly eroding terrains like Melamchi. The importance of temperature is not directly inferred from these models, requiring further study.

# Contents

<b>Abstract</b>	i
<b>1 Introduction</b>	1
<b>2 Study Area</b>	6
2.1 <i>Geological Setting</i> . . . . .	6
2.2 <i>Climate</i> . . . . .	6
<b>3 Data Collection and Measurement</b>	9
3.1 <i>Field Sampling</i> . . . . .	9
3.2 <i>Major and Trace Element Analysis</i> . . . . .	9
<b>4 Methods and Models for Analysis</b>	10
4.1 <i>Rain and Hydrothermal Correction</i> . . . . .	10
4.2 <i>Identifying the Weathering Reaction</i> . . . . .	10
4.3 <i>One-Dimensional Reactive Transport Models</i> . . . . .	13
4.4 <i>Estimates of Uncertainty</i> . . . . .	20
<b>5 Results: Spring Chemistry and Residence Time</b>	21
5.1 <i>Traverse 1</i> . . . . .	21
5.2 <i>Traverse 2</i> . . . . .	22
5.3 <i>Traverse 3</i> . . . . .	23
5.4 <i>Traverse 4</i> . . . . .	24
5.5 <i>Traverse 5</i> . . . . .	26
5.6 <i>Results Table</i> . . . . .	27
5.7 <i>Time Series Trends</i> . . . . .	34

<b>6 Discussion</b>	<b>36</b>
<i>6.1 Explaining Traversal Variations in Chemistry</i>	36
<i>6.2 Residence Time Agreement with Gas Ages</i>	37
<i>6.3 Free Energy Calculations Concur on Far From Equilibrium State</i>	38
<i>6.4 Model Sensitivity to Concentration</i>	43
<i>6.5 Is the Rate Constant Used Appropriate?</i>	45
<b>7 Conclusions and Future Work</b>	<b>47</b>
<b>Appendix 1: Rain and Hydrothermal Correction Equations</b>	<b>54</b>
<b>Appendix 2: Derivation of Reactive Transport Models</b>	<b>56</b>

# Acknowledgements

This thesis would not have been possible without the amazing help from my supervisor, Ed Tipper. Mike Bickle, Al Knight, and Morag Hunter have also been instrumental in guiding me through this Master's year. Thank you also to Alex Piotrowski for guidance in lab-work, and to Zara Crapper for being a great field partner. Thank you to Girton College, the University of Cambridge, and the NSF for providing funding for fieldwork to Nepal. To my friends and peers, thank you for supporting me as always. A Mamma, Papà, e alla Virgi, grazie di tutto come sempre. To Beth, thank you for being you, and always being there for me.

# Declaration

I declare that the submitted work is my own, except where acknowledgement is given to the work of others or to work done in collaboration. I declare that I have read and understood the department of Earth Sciences statement on plagiarism and that my work could be tested using automated plagiarism software.

*Signed:*



**Giovanni Bernardi**

# Word Count

The total word count, excluding abstract, figures, tables, references, and appendices is 7485 words.

# Nomenclature

**Kinetically limited:** When there is an abundant mineral supply, and weathering is limited by the kinetics of reactions.

**Chemical Equilibrium:** When the forward and backward rates of a reaction are equal.

**Reactive Transport Models:** Models that simulate chemical reactions in time and space.

**Runoff:** Amount of water draining from a catchment per unit area.

**Discharge:** Amount of water per unit time flowing through a water body.

**Fontorbe Model:** Reactive Transport Model that assumes a constant rate of reaction.

**Maher Model:** Reactive Transport Model that assumes reaction rate depends on the concentration as it approaches equilibrium.

**Residence Time:** Amount of time a given water packet spends in the subsurface before emerging at a spring.

**Flow Path Length:** Distance water travels through the subsurface.

**Porosity:** Void space in a rock.

**HHCS:** Higher Himalayan Crystalline Sequence.

**LHS:** Lesser Himalayan Sequence.

**MCT:** Main Central Thrust, Himalayan fault zone separating the HHCS from the LHS.

**ISM:** Indian Summer Monsoon.

**Lapse Rate:** The rate at which atmospheric temperature decreases with elevation.

**Modal Decomposition:** Mathematical method used for dimensionality reduction. Used to estimate molar proportions of minerals contributing to the dissolved load.

**Free Energy:** Energy available to do work in a system.

**DSi:** Dissolved silicon in water. Commonly in the form of  $\text{H}_4\text{SiO}_4$ .

# 1 Introduction

Silicate weathering, whereby silicate minerals are dissolved by carbonic acid, sequesters atmospheric CO<sub>2</sub> over millions of years, and is proposed to be the dominant mechanism by which global climate is controlled on these timescales. As water passes through the subsurface, it interacts with the surrounding rock. This causes the addition of solute species to the groundwater, and the formation of stable secondary minerals through the dissolution of primary minerals. Large mountain ranges in particular are thought to be most sensitive to weathering (Tipper et al., 2006). The Himalayan mountain range spans more than 590,000 km<sup>2</sup>, and is the source of major rivers, including the Ganges, Brahmaputra, and Indus. Silicate weathering in the Himalayas as a result of their uplift and erosion in the Cenozoic may have contributed significantly to the global cooling over the past 40 million years (Raymo & Ruddiman, 1992; West et al., 2005; Kump et al., 2000). Clearly, understanding the strongest control on weathering in these key regions for the global carbon cycle is of utmost importance to inform climate policy.

The dissolution kinetics of the silicate rocks in Himalayan catchments are thought to depend on both temperature and runoff because the weathering reactions have not gone to completion. Weathering regimes can be classified as either transport-limited or kinetically-limited (West et al., 2005). That study classifies the two regimes based on the rate of erosion in the catchment. In low erosion rate settings, weathering is transport-limited: weathering rate is proportional to the material eroded, so is limited by the transport of material to the weathering interface. In high erosion rate settings, there is an abundant mineral supply and so only reaction kinetics stand in the way of the weathering reaction. Rapidly eroding catchments like Melamchi in North-East Nepal are likely kinetically-limited (Stallard & Edmond, 1983, see Figure 1). In regions like Melamchi, silicate weathering reactions are thought to be more sensitive to temperature than runoff.

Rates of reaction play a crucial role in chemical weathering reactions. These comprise both dissolution and precipitation, and chemical equilibrium is defined as that state where

these are balanced and equal. The rate of weathering is dependent on the mineralogy of the rock. Different minerals weather at different rates. This also depends on the mineral surface area available for reaction, which is one of the most underconstrained aspects of weathering models (White & Brantley, 2003). The most reactive minerals will disproportionately contribute to the solute load of the water (Shand et al., 1999). Therefore, understanding the primary mineral reaction to model is key when quantifying weathering in a catchment. Reaction rate constants are observed to be different depending on whether they are measured in the field or in a laboratory (Maher, Steefel, et al., 2009). This difference has been explained by 'extrinsic' qualities that are variable in the field, such as permeability, mineral/fluid ratios, and different surface areas available to react (White & Brantley, 2003). The rate constant of a system has also been linked to the free energy of the system, with laboratory rates being calculated significantly further away from equilibrium than field rates (Kampman et al., 2009). In other words, field localities are thought to be closer to equilibrium than laboratory-derived constants might suggest.

In the Melamchi catchment, only weathering through carbonic acid is considered. Weathering through sulfuric acid also significantly contributes to the global weathering budget, but its impact is not considered in this study because the marine deposits required for its formation are not present in the Melamchi region (Bufo et al., 2021).

Rain is a key driver of groundwater flow. The Indian Summer Monsoon (ISM) in Nepal is characterised by a strong seasonal reversal of winds, which brings heavy rainfall to the region during the summer months, and dry conditions during the winter (Bookhagen & Burbank, 2010). The monsoon brings a large amount of precipitation to the region. Seasonal variation in precipitation also translates to a variation in runoff, whereby this is twelve times stronger during the monsoon than during the dry season (Sharma, 1997).

Changes in climate contribute to changes in the monsoonal system dynamics, which in turn affect weathering rates. The start of the monsoon has not changed in Nepal, but the end has been delayed. This has led to more intense precipitation on a per day basis, which

is detrimental for crops in the winter season due to lack of moisture. Intense precipitation is also considered the main climatic cause of flooding (Panahi et al., 2015; Baniya et al., 2024). "One-off" landslide events transport as much as four times the flux of sediment deposited in the valley in a year (Chen et al., 2023). These events are thought to be increasing in frequency over recent years as a result of climate change, increasing the erosion rate in these areas (Adhikari et al., 2023). Increased erosion rates drive the Melamchi catchment to more kinetically-limited weathering.

These variables can be integrated into reactive transport models. Reactive transport models are widely used in Earth Sciences to simulate the flow of groundwater through the subsurface (Bethke, 2011). These models can be used to simulate chemical weathering reactions through one-dimensional flow paths based on a few key parameters, which make up the "weathering fingerprint" of a catchment. Models built on different assumptions on weathering control will produce different results. Some of these models are built on the assumption that kinetic weathering rates change with the amount of runoff and the approach to chemical equilibrium, whilst others assume they are constant. The former, "Maher models" (from now on, after Maher (2011)) propose that silicate weathering is most sensitive to runoff. Maher (2011) uses this model to suggest that all weathering paths approach equilibrium. Conversely, the latter "Fontorbe models" (from now on, after Fontorbe et al. (2013)), do not assume a strong runoff control, and are therefore more sensitive to temperature than runoff compared to the Maher models. This study looks at Melamchi to act as a case study for Himalayan weathering.

Residence time is a critical control on how likely weathering is to approach equilibrium. Residence time, also called the advective age, is defined by how long a given water packet spends from rain recharge into groundwater to exiting at a spring (McCallum et al., 2015). Estimation of residence time from the Maher and Fontorbe models using measured spring chemistry in Melamchi can be used to determine which model is most appropriate, and therefore what factors control weathering in Melamchi. The weathering fingerprints of these catchments contain many unknowns, namely the residence time of the water, min-

eral surface areas, rate of reaction, and extent to which equilibrium is reached. Spring chemistry is reflective of the weathering processes that occur in the subsurface, and can therefore be used to estimate these fingerprint parameters; note, however that it is unclear how much of the water flows through the spring system. This proportion is likely only a fraction of the total. Understanding residence time in particular is important because the geochemical and biogeochemical reactions that contribute to the solute load during weathering are time-dependent; generally, longer residence times promote greater solute accumulation in the water (Berner, 1978). These geochemical reactions are also controlled by the reaction rate, which is thought to vary as equilibrium is approached (White & Brantley, 2003; Maher, 2011). Therefore, an understanding of residence time will provide insight into how long weathering reactions take place in a given catchment, whether they reach equilibrium, and what this means for the carbon cycle as a whole. Residence time will also inform the effects of drought in a catchment. Long residence times are likely to be more resilient to periods without rainfall (Atwood, 2023). Calculating residence time using the spring chemistry in Melamchi will allow the assumptions underlying the two models to be tested, and assess their applicability to a real-world catchment.

From the model comparison will come a better understanding of fluid residence times in Himalayan catchments, for which tracer data is already commonly used to infer how long a water packet spends in the subsurface (Atwood, 2023). Previous studies on Melamchi have used CFC and SF<sub>6</sub> gases to determine a mean age on the order of ten years for groundwater at the base of the catchment ridge (Atwood, 2023, Traverse 3 in Figure 1). These ages are significantly older than the estimates from Andermann et al. (2012); that study uses precipitation and discharge relationships in the Himalayas to suggest that there is a three month lag in the response of the river to precipitation. This suggests the samples collected in Melamchi are only sampling part of the groundwater system. Estimated residence times from Atwood (2023) differ widely depending on the proxy used. This is likely due to the difficulty of sampling water uncontaminated by the atmosphere (McCallum et al., 2015). Using the chemical composition of the water will provide a different way of obtaining residence times, and give a benchmark for the tracer data, which is often reported

to be limited in its application (McCallum et al., 2015). If the residence time of a particular water packet is long enough, the reaction will reach chemical equilibrium, meaning the free energy of the system will be close to zero (Kampman et al., 2009). Comparison of these residence times with separate estimates of free energy derived from the measured concentration of springwater in the catchment will test the validity of the two models and their assumptions. Finally, this will help to inform whether weathering in catchments like Melamchi is most strongly controlled by temperature or runoff.

In this study, spring and rain samples from the Melamchi region of Nepal are used as a case study to investigate the weathering rates in a kinetically-limited catchment (see Figure 1). The sample dataset consists of 372 samples spanning five field campaigns over six years (2018-2024) completed as part of an NSF research project, as well as more recent year-long bi-weekly timeseries data from stream and spring samples in sites across the catchment. Of those, 68 were collected in September 2024 by a team comprising myself and researchers from the University of Cambridge and Kathmandu University for this study. This dataset comprises major ion concentrations, alkalinity, and radiogenic strontium isotopes from the Melamchi catchment.

## **2 Study Area**

The Melamchi-Indrawati catchment (85.441 - 85.601 E, 27.822 - 28.157 N) study area ranges from 790 to 5700 m a.s.l. (metres above sea level). The Melamchi River is a tributary of the larger Indrawati River and runs through the catchment draining an area of 325km<sup>2</sup>. The catchment has a mean slope of 20% and a mean elevation of 2400m (see Figure 1).

### **2.1 Geological Setting**

The overall geology is largely comprised of silicate metamorphic rock. The geology of Melamchi is characterised by banded gneiss, feldspathic schist and laminated quartzite of the Higher Himalayan Crystalline Sequence (HHCS) (Dhital (2015); see Figure 1). To the south of the confluence of the Melamchi River to its parent Indrawati river lies the Main Central Thrust (MCT) which separates the HHCS from the Lower Himalayan Sequence (LHS) (Dhital, 2015; Graf et al., 2023).

### **2.2 Climate**

Annual mean temperatures in the Melamchi Khola Catchment range from  $\approx 24^{\circ}\text{C}$  at base elevation to  $\approx 8^{\circ}\text{C}$  at highest elevation sampled (3200 m a.s.l.; see Figure 2). Recorded temperatures at the end of the spring flow paths vary with the season, being coldest in November. All seasons show a temperature decrease with increasing elevation, consistent with the free-air moist adiabatic lapse rate, which is =  $6.5^{\circ}\text{C}/\text{km}$  (Barry & Chorley, 2009). This suggests that the springs are not advecting significant geothermal heat. The area features a high erosion rate and a large topographic gradient. This corresponds to a large temperature gradient contributing to tropical and alpine climates close to one another (Kattel et al., 2013). The westerly winds typical of this latitude are responsible for the dry season in the Himalayas (Bookhagen & Burbank, 2010). This temperature gradient reverses in the winter, when the oceans are warm and the High Himalaya is cold. The Melamchi Khola catchment receives over 80% of its rainfall during the monsoon (Bookhagen & Burbank, 2010).

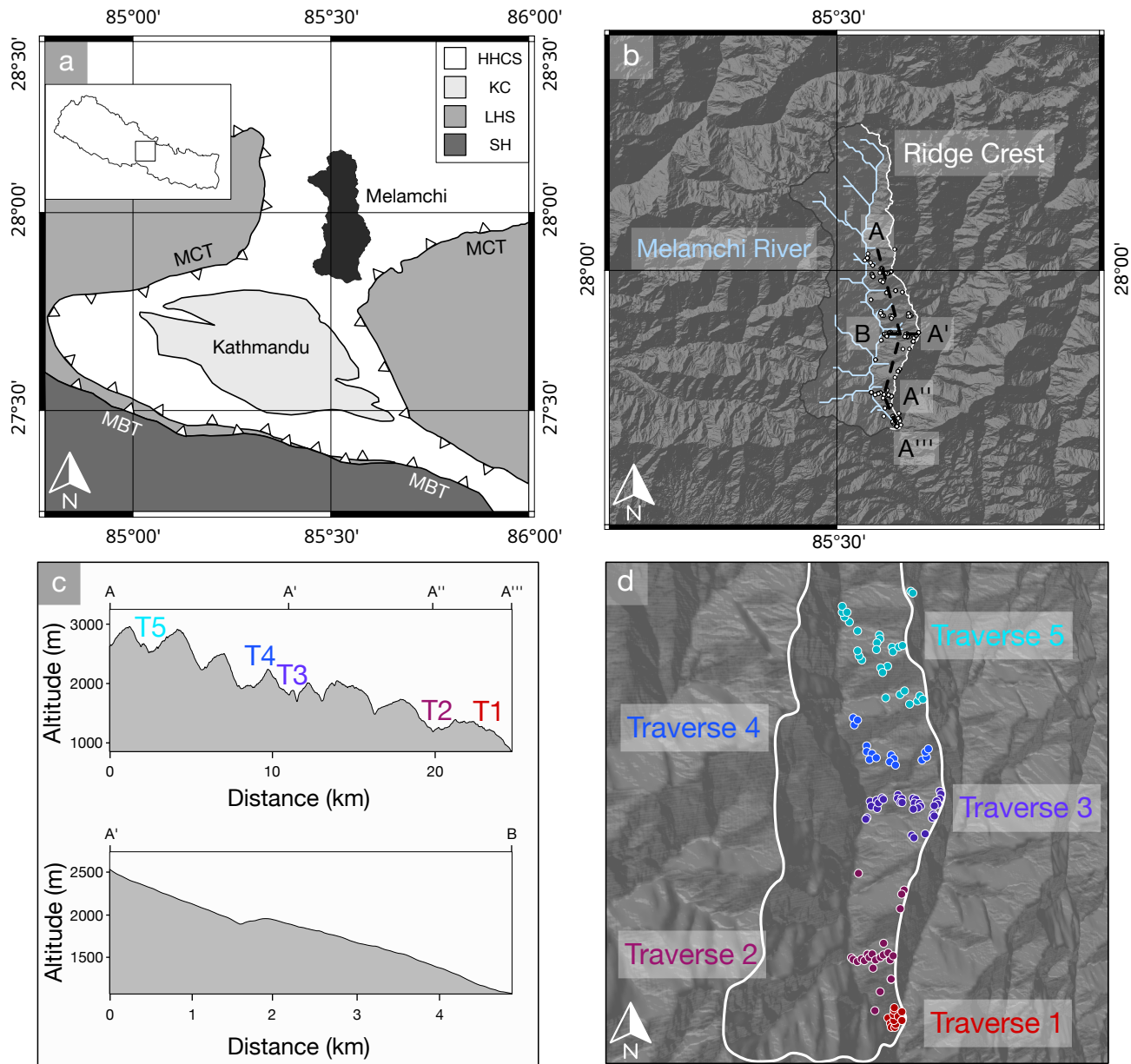


**Figure 1:** Maps representing the Melamchi Catchment. (a) The location of the Melamchi Catchment in Nepal. Geological setting is shown, adapted from Dhital (2015). Melamchi sits in the HHCS. (b) The Melamchi Catchment with the Melamchi River flowing from North to South highlighted in blue. DEM data is from NASA Space Systems (2018). (c) Topographic profiles along and across the ridge in Melamchi, corresponding to the lines in (b). (d) Spatial extent of samples in each traverse.

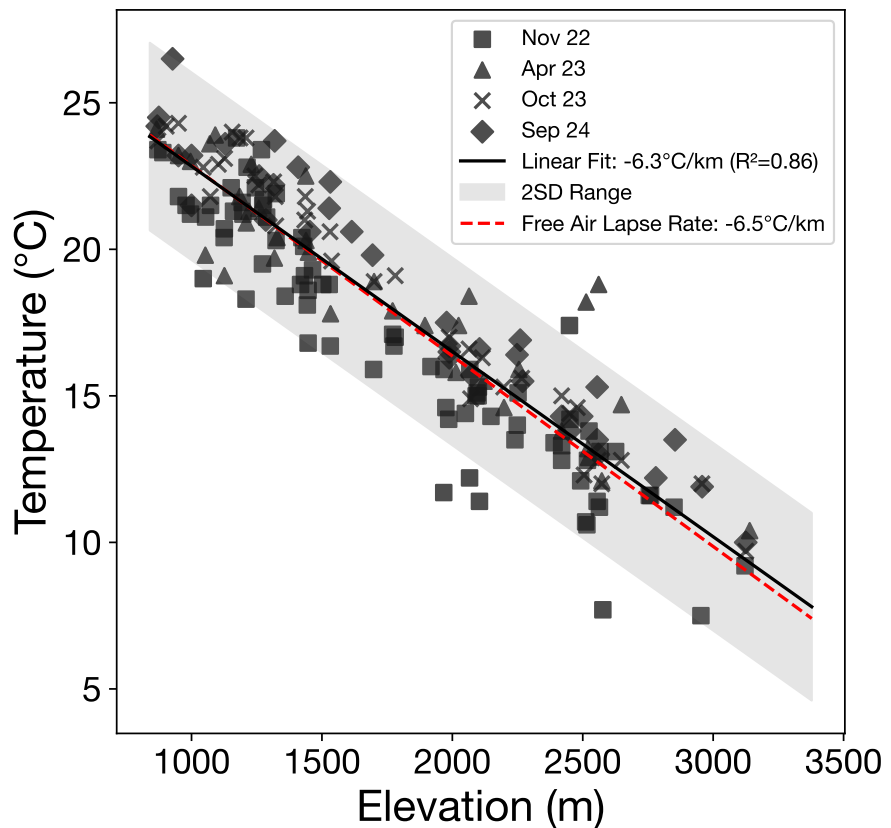


Figure 2: Temperature against elevation for each sampled season, with grey band representing two standard deviations from the mean. Lapse rate is consistent with the free air adiabatic lapse rate within error.

### **3 Data Collection and Measurement**

#### **3.1 Field Sampling**

Both springs and rain were sampled in the field. Springs were sampled according to locations visited in past expeditions. Rain was collected in a rain gauge along several transects. Six aliquots were collected for each spring for anion, cation, titration, DIC, isotope and archive purposes. Both water bodies were measured in the field for temperature, pH and TDS on Hanna Instruments HI-991300 and EXTECH DO700. Samples were also titrated using a Hach digital titrator with 0.0625M HCl to calculate the alkalinity of the water following the Gran Method (Gran, 1952). Titrations were done on 50ml aliquots, 24 hours within having been collected. Rain samples had a smaller yield and so only three aliquots were collected, for cation and anion, isotope and archive purposes. Both water body types were filtered through a 0.2 $\mu$ m PES membrane in a filtration unit prior to bottling. Cation and archive samples were acidified with concentrated HNO<sub>3</sub> to give a pH of ~2, keeping the cations in solution.

#### **3.2 Major and Trace Element Analysis**

Cation concentrations were determined using an Agilent Technologies 5100 Inductively-Coupled Plasma Optical Emission Spectrometer (ICP-OES) using a calibration line made from a Nepalese spring stock solution. Anion concentrations were determined using a Dionex Ion Chromatography System (ICS) 5000 series against the Battle-O2 standard calibration line. Associated uncertainties range between 5-10% for cations and anions.

## **4 Methods and Models for Analysis**

### **4.1 Rain and Hydrothermal Correction**

Rain input is a significant factor in the chemical composition of groundwater and rivers. Most chloride found in these water bodies is thought to be due to rainwater input (Drever, 1997). It is standard practice to correct for this input using the measured concentrations of chloride in the rain. Rain samples collected in the September 2024 season are used for this correction, detailed in Appendix 1. Once the samples have been corrected for rain input, the remaining chloride is assumed to be derived from hydrothermal signatures encountered in the flow path. Spring waters are also therefore corrected for hydrothermal input using the most chloride-rich springs, so that the concentrations used for modelling are strictly derived from weathering reactions.

### **4.2 Identifying the Weathering Reaction**

The first step towards quantifying the extent to which chemical weathering reactions have gone to completion is to discern what reaction is taking place. In principle this is as simple as knowing what minerals are dissolving (the "forward" reaction) and which are precipitating (the "backward" reaction). Modal decomposition is a mathematical method that can be applied to consider several minerals that could be dissolving and/or precipitating, and how they contribute to the spring chemistry (Garrels & Mackenzie, 1967; Drever, 1997). Note that this calculation can only be done if the number of components is the same as, or greater than the number of minerals.

$$\begin{array}{ccccccc}
& Biot & Plag & Calc & Smec & Kaol & KSpar & Spring(\mu\text{mol/l}) \\
Si & \left( \begin{array}{cccccc} a_{11} & a_{12} & a_{13} & a_{14} & a_{15} & a_{16} \end{array} \right) & \left( \begin{array}{c} x_{Biot} \\ x_{Plag} \\ x_{Calc} \\ x_{Smec} \\ x_{Kaol} \\ x_{KSpar} \end{array} \right) & = & \left( \begin{array}{c} b_1 \\ b_2 \\ b_3 \\ b_4 \\ b_5 \\ b_6 \end{array} \right) \\
Al & \left( \begin{array}{cccccc} a_{21} & a_{22} & a_{23} & a_{24} & a_{25} & a_{26} \end{array} \right) & & & & & \\
Mg & \left( \begin{array}{cccccc} a_{31} & a_{32} & a_{33} & a_{34} & a_{35} & a_{36} \end{array} \right) & & & & & \\
Ca & \left( \begin{array}{cccccc} a_{41} & a_{42} & a_{43} & a_{44} & a_{45} & a_{46} \end{array} \right) & & & & & \\
Na & \left( \begin{array}{cccccc} a_{51} & a_{52} & a_{53} & a_{54} & a_{55} & a_{56} \end{array} \right) & & & & & \\
K & \left( \begin{array}{cccccc} a_{61} & a_{62} & a_{63} & a_{64} & a_{65} & a_{66} \end{array} \right) & & & & & 
\end{array}$$

Matrix algebra facilitates the calculations of the molar proportions of mineral added to the water. Given known matrices  $A$  and  $B$ , where  $A$  represents the stoichiometric quantities of elements in a mineral, and  $B$  the concentrations of elements in the water:

$$AX = B \quad (1)$$

$$X = A^{-1}B \quad (2)$$

The matrix  $X$ , corresponding to molar proportions of mineral added to the water, can then be calculated, under the assumptions that all minerals dissolve in a congruent fashion. Modal decomposition for spring waters was performed according to stoichiometric proportions from Bickle et al. (2015).

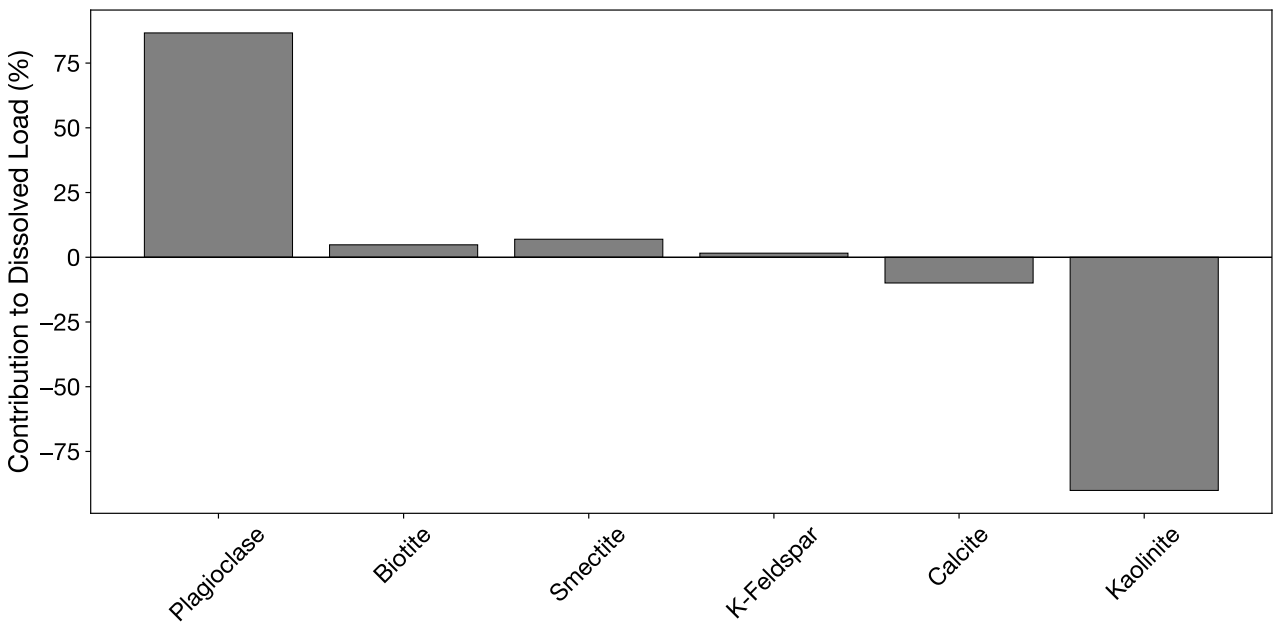
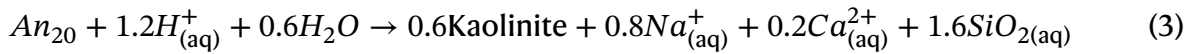
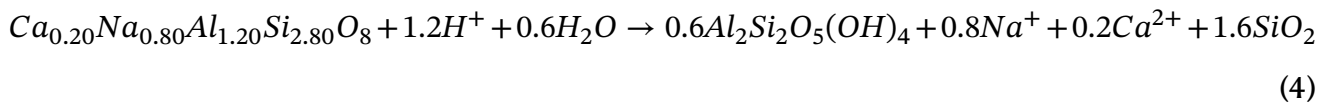


**Figure 3:** Modal Decomposition results averaged over all springs. y-axis corresponds to modal proportion of mineral contributing to the dissolved (measured) load. Negative y-space indicates the mineral is involved in the backward reaction.

Figure 3 suggests that the major phase being dissolved is plagioclase feldspar (the forward reaction) and the major phase being precipitated is kaolinite (the backward reaction). Plagioclase feldspar is made up of a solid solution of albite ( $\text{NaAlSi}_3\text{O}_8$ ) and anorthite ( $\text{CaAl}_2\text{Si}_2\text{O}_8$ ) (Henry et al., 1982). A plagioclase with composition  $\text{An}_x$  (or equivalently  $\text{Ab}_y$ ) is made up of  $x$  mol % anorthite and  $y$  mol % albite. The primary composition of plagioclase in the area averages to  $\approx \text{An-20}$  with considerable scatter in the data (Bickle et al., 2015; Knight et al., 2024). The joint plagioclase to kaolinite reaction is given by the following equation (written so that aluminium is conserved):



Or



## 4.3 One-Dimensional Reactive Transport Models

Reactive transport models can be used to estimate the residence time of water in a catchment. These models are widely used in applied fluid dynamics and various fields within Earth Sciences. They aim to track chemical reactions occurring at each spatial point, accounting for the movement of reactants to and reaction products away from those points (Bethke, 2011). The basic form of a reactive transport model is a partial differential equation that describes the transport of solutes and the reactions that occur between them. For reacting solutes, concentration changes over time are governed by transport rates and the relative rates of dissolution and precipitation (Bethke, 2011). These models simplify a real world three-dimensional catchment into one-dimensional flow paths. The proposed equations can be complex, but in simple cases a species of concentration  $C_i$  can be modelled to follow a first-order rate law, generally represented by:

$$\frac{\partial C_i}{\partial t} = \mathcal{O}_T(C_i) + \mathcal{O}_R(C_i) \quad (5)$$

Where  $\mathcal{O}_T$  and  $\mathcal{O}_R$  are the transport and reaction operators, respectively (Bethke, 2011). Transport operators are derived from the divergence principle; this states that the rate of change in the concentration of a component over time depends on how the advective and dispersive fluxes vary spatially and temporally. Depending on the hypothesis supported, equation 5 can be modified accordingly. The following sections will discuss two models with their own versions of equation 5.

### The Role of Porosity and Permeability

Estimation of porosity and permeability is essential for understanding the extent of weathering in a catchment. Understanding how open a rock is to water flow and reaction can constrain the reactive transport models used to estimate residence time. Porosities vary widely across a catchment depending on the rock type encountered (Singh et al., 1987; David et al., 1994). Porosity also increases as a rock becomes more weathered (Marques et al., 2010). Note that in the following models, the porosity value is taken to be an average over a given depth in the subsurface. In Earth Sciences, models of fluid flow – whether in

the subsurface or deep within the Earth – are typically categorized based on whether the flow occurs through a porous medium or within large open channels (Pedrazas et al., 2021; Maher, 2011; Kelemen et al., 1995; Jackson et al., 2018). This remains an open debate beyond the scope of this study (though note that flow paths are depicted as "channels" to facilitate the explanation of reactive transport, see Figure 4). Hence, the porosity value used for residence time calculation in the reactive transport models is assumed to be an average. This allows for both types of flow to be plausible, whether in a highly porous medium or large channels surrounded by less porous rock. Also note that these models do not directly consider permeability.

## Model Motivation

As discussed in the Introduction, there are different hypotheses regarding the major controls on chemical weathering. This study will contrast one model that assumes kinetic weathering rates are constant, with another which assumes the rates change with the amount of runoff and the approach to chemical equilibrium. These two, Fontorbe and Maher models, respectively follow different hypotheses regarding the strongest control on weathering as a result of their assumptions. The Fontorbe model exhibits greater sensitivity to temperature than the Maher model which is more influenced by runoff. The benchmark for a model's effectiveness will be how well it can predict residence times compared to previous studies on gas tracers. Assumptions and constraints will be compared and contrasted, and their results used to inform the calculation of rates of reaction and approach to equilibrium in Melamchi. For both models, the element used to estimate residence times is dissolved silicon (DSi). The element silicon is present in both dissolution and precipitation reactions, so it is applicable to the Maher model which considers both reactions. Furthermore, DSi is what both models were built for in their respective original studies. Lastly, both models use the same reaction rate constant  $k = 10^{-15} \text{ mol m}^{-2} \text{ s}^{-1}$ ; this is considered a value appropriate to use for close to equilibrium settings.

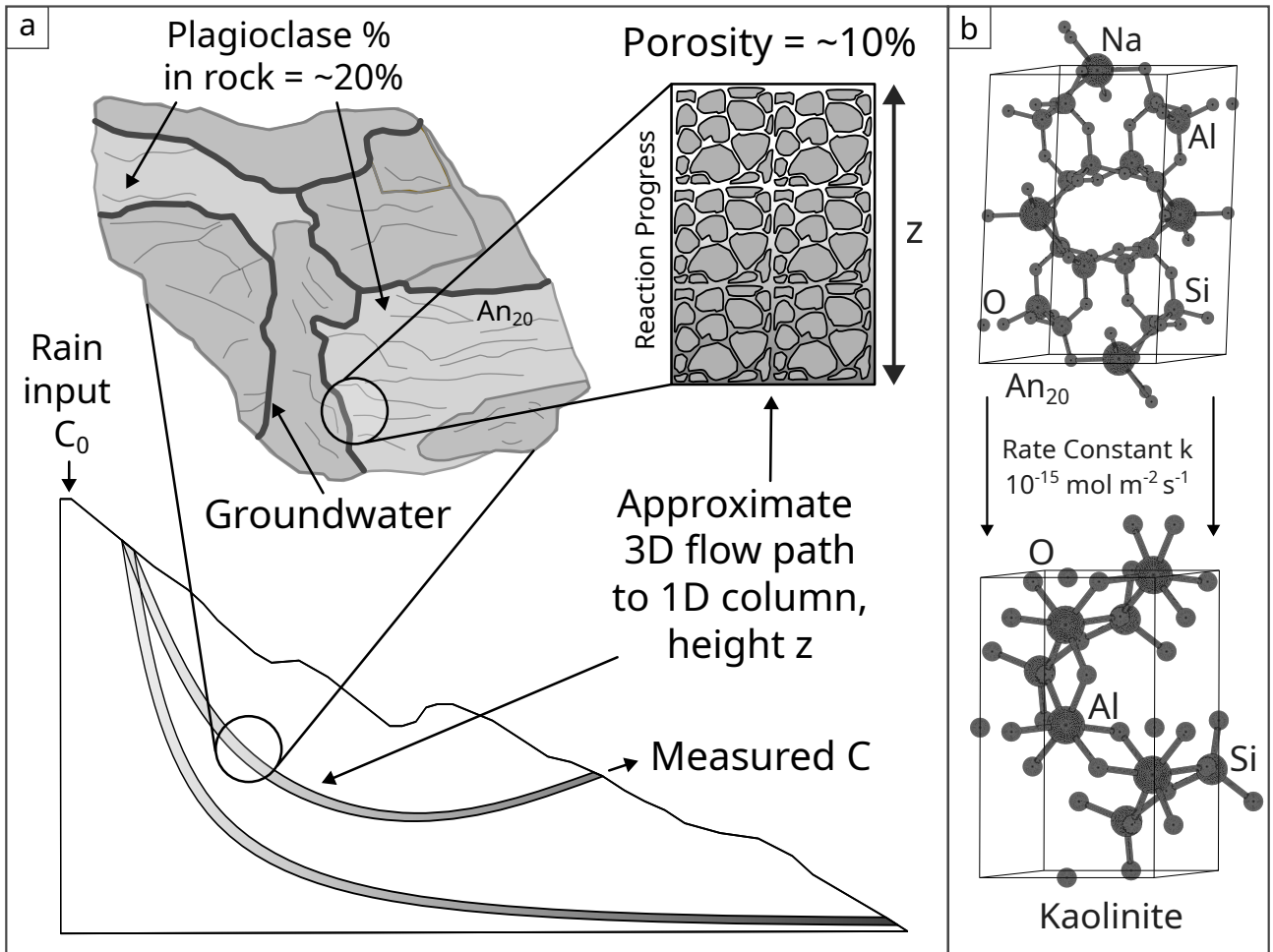


Figure 4: (a) Illustration showing workflow performed in reactive transport models. Sketch shows different parameters used, such as the rain input at the top of the catchment used for the initial " $C_0$ " concentration, the plagioclase percentage in the rock as well as the porosity. (b) Mineral ball and spoke models showing the dissolution of plagioclase and precipitation of kaolinite. Ball and spoke models adapted from Vaitkus et al. (2023), Gražulis et al. (2015), Downs & Hall-Wallace (2003).

## Fontorbe et al. (2013) - Model Equations

Fontorbe et al. (2013) investigates silicon isotopic composition in the Ganges River, assuming constant reaction rates along flow paths (see Appendix 2 for a full derivation, and Table 1 for a list of parameters used). This model was initially constructed to reproduce DSi concentration and  $\delta^{30}\text{Si}$  in the Ganges, but is being repurposed in a novel fashion for this study. The first-order differential equation governing transport and reaction is given as:

$$\phi \frac{\partial C}{\partial t} = -\omega \phi \frac{\partial C}{\partial z} + R_n(1 - f) \quad (6)$$

Where  $C$  is the elemental concentration in  $\mu\text{mol/L}$ ,  $\omega$  is the fluid velocity in  $\text{m/s}$ ,  $\phi$  is the rock porosity,  $z$  is a position along the flow path in  $\text{m}$ ,  $R_n$  is the rate of reaction in  $\text{mol/m}^3/\text{s}$ , and  $f$  is the fraction of Si present in the dissolved load that is reprecipitated in the back reaction. The equation can be nondimensionalised using the Damköhler number ( $N_D$ ), which describes the relative importance of kinetic vs transport-controlled settings (Bethke, 2011):

$$N_D = \frac{R_n h}{\phi C_0 \omega} \quad (7)$$

Where  $h$  is the full length of the flow path (i.e. the maximum  $z$ ). For a flow path averaged as stated above, the porosity is so small that the relative fractions of reacting phases do not change with time as much as the advective and transport terms. As such, the steady state ( $\partial C / \partial t = 0$ ) assumption can be used and the concentration at the end of the flow path can be rearranged to give the residence time  $T_f$ :

$$T_f = \frac{(C - C_0)\phi}{(1 - f)R_n} \quad (8)$$

<b>Fontorbe et al. (2013) - Model Parameters</b>			
<b>Parameter</b>	<b>Definition</b>	<b>Units</b>	<b>Formula (Value)</b>
$\phi$	Porosity	-	0.1*
$\omega$	Fluid velocity	m/s	Variable
$h$	Length of flow path	m	Variable
$C$	Concentration end of flow path	$\mu\text{mol/L}$	Variable
$C_0$	Initial concentration	$\mu\text{mol/L}$	Rain Input
$f$	Fraction reprecipitated	-	0.5*
$N_D$	Damkohler Number	-	$N_D = \frac{R_n h}{\phi C_0 \omega}$
$T_f$	Residence time	s	$T_f = \frac{h}{\omega \phi}$
$R_n$	Reaction rate	$\text{mol}/\text{m}^3/\text{s}$	$\rho \cdot 10^6 \cdot k \cdot S \cdot X$
$k$	Dissolution rate constant	$\text{mol}/\text{m}^2/\text{s}$	$10^{-15}*{}$
$S$	Specific surface area	$\text{m}^2/\text{g}$	0.1*
$\rho$	Plagioclase density	$\text{g}/\text{cm}^3$	2.7*
$X$	Volume fraction of mineral in rock	$\text{g}_{\text{min}}/\text{g}_{\text{rock}}$	0.2*

Table 1: Key parameters and definitions for the Fontorbe model. \* - Values used for calculation.

## Maher (2011) - Model Equations

This model is built in accordance with the principle that the main control on silicate weathering is runoff. The model is based on the assumption that the reaction rate decreases linearly with approach to equilibrium, and that all weathering paths approach equilibrium. The model is initially set out in Maher (2011) and further developed in Maher & Chamberlain (2014). The motivation behind the hydrological control on weathering is based on sensitivity analyses of real catchment data on one-dimensional reactive transport models which suggest that porosity, mineral surface area, and temperature have no consistent correlation with water composition (Maher, 2011). See Appendix and Table 2 for a full derivation and the model parameters respectively. The model begins with the following representation of the concentration of a solute in a fluid flow path:

$$\frac{dC}{dt} = -\frac{q}{\theta} \frac{dC}{dz} + \sum_i \mu_i R_{d,i} \left(1 - \left(\frac{C}{C_{eq}}\right)^{n_i}\right)^{m_i} - \sum_i \mu_i R_{p,i} \left(1 - \left(\frac{C}{C_{eq}}\right)^{n_i}\right)^{m_i} \quad (9)$$

Where  $C$  is the concentration in  $\mu\text{mol/L}$ ,  $q$  is the flow rate in  $\text{m/s}$ ,  $\theta$  is the volumetric water content in  $\text{m}^3$ ,  $z$  is the position along the flow path in  $\text{m}$ ,  $\mu$  is the stoichiometric coefficient dependent on the reacting minerals,  $R$  is the rate of reaction for dissolution and precipitation respectively in  $\text{mol/L/s}$ ,  $C_{eq}$  is the equilibrium concentration in  $\mu\text{mol/L}$ , and  $n$  and  $m$  are non-linear parameters (Maher, 2011). For a given packet of water,  $R_n$  is:

$$R_n = R_d - R_p \quad (10)$$

$$\frac{dC}{dt} = R_n \left(1 - \frac{C}{C_{eq}}\right) \quad (11)$$

Where  $R_d$  and  $R_p$  are the rates of dissolution and precipitation respectively. This can be solved for concentration, and rearranged for residence time to obtain:

$$T_f = \frac{C_{eq} \cdot (C - C_0)}{e^2 R_n (C_{eq} - C)} \quad (12)$$

The  $e^2$  term appears because of the Maher & Chamberlain (2014) formulation to understand over which length scale water compositions reach equilibrium. The model is built so that these are theoretically infinite, so  $e^2$  is used as a small difference between infinity and the finite distances that occur in natural systems in order to make the model applicable to the real world.

<b>Maher (2011) - Model Parameters</b>			
<b>Parameter</b>	<b>Definition</b>	<b>Units</b>	<b>Formula (Value)</b>
$\phi$	Porosity	-	0.1*
$h$	Length of flow path	m	Variable
$\theta$	Volumetric water content	$m^3$	Variable
$q$	Flow rate	m/s	Variable
$C_{eq}$	Equilibrium concentration	$\mu\text{mol/L}$	Max Catchment
$C_0$	Initial concentration	$\mu\text{mol/L}$	Rain Input
$R_n$	Net reaction rate	$\text{mol/L/s}$	$\rho \cdot 10^6 \cdot k \cdot S \cdot X$
$\rho$	Plagioclase density	$\text{g/cm}^3$	2.7*
$k$	Dissolution rate constant	$\text{mol/m}^2/\text{s}$	$10^{-15}*^*$
$S$	Specific surface area	$\text{m}^2/\text{g}$	0.1*
$X$	Volume fraction of mineral in rock	$\text{g}_{\text{min}}/\text{g}_{\text{rock}}$	0.2*
$\tau$	Scaling factor	-	$\tau = e^2$
$D_w$	Damkohler Coefficient	$\text{m}^2/\text{s}$	$D_w = \frac{L\phi R_n}{C_{eq}}$
$T_f$	Residence time	s	$T_f = \frac{h\phi}{q}$

Table 2: Key parameters and definitions for the Maher model. \* - Values used for calculation.

## 4.4 Estimates of Uncertainty

Uncertainties were estimated using a Monte Carlo approach with 1000 simulations, assuming a normal distribution. Initial uncertainties are detailed in Table 3. Both observed and estimated parameters include associated uncertainties. After running multiple simulations, the resulting distribution represents the potential range of values for the chosen parameters.

Parameter Definitions and Initial Uncertainties				
Parameter	Definition	Units	Value	Uncertainty
$\phi$	Porosity	-	0.1	$\pm 10\%$
$C_{eq}$	Equilibrium DSi concentration	$\mu\text{mol/L}$	869	$\pm 10\%$
$C_0$	Initial DSi concentration	$\mu\text{mol/L}$	95	$\pm 10\%$
$\rho$	Plagioclase density	$\text{g/cm}^3$	2.7	$\pm 10\%$
$k$	Dissolution rate constant	$\text{mol/m}^2/\text{s}$	$10^{-15}$	$\pm 10\%$
$S$	Specific surface area	$\text{m}^2/\text{g}$	0.1	$\pm 10\%$
$X$	Volume fraction of mineral in rock	$\text{g}_{\text{min}}/\text{g}_{\text{rock}}$	0.2	$\pm 10\%$
$f$	Fraction reprecipitated	-	0.5	$\pm 10\%$
$\Delta G^0$	Standard Gibbs Free Energy	$\text{kJ/mol}$	$-\text{RT}\ln K^*$	$\pm 10\%$

Table 3: Key parameters, definitions, and initial uncertainties to be propagated. \* - Uncertainty associated with temperature and K calculated from the python pygcc package using The Geochemist's Workbench® RxN program (Bethke, 2011; Awolayo & Tutolo, 2022).

## 5 Results: Spring Chemistry and Residence Time

### 5.1 Traverse 1

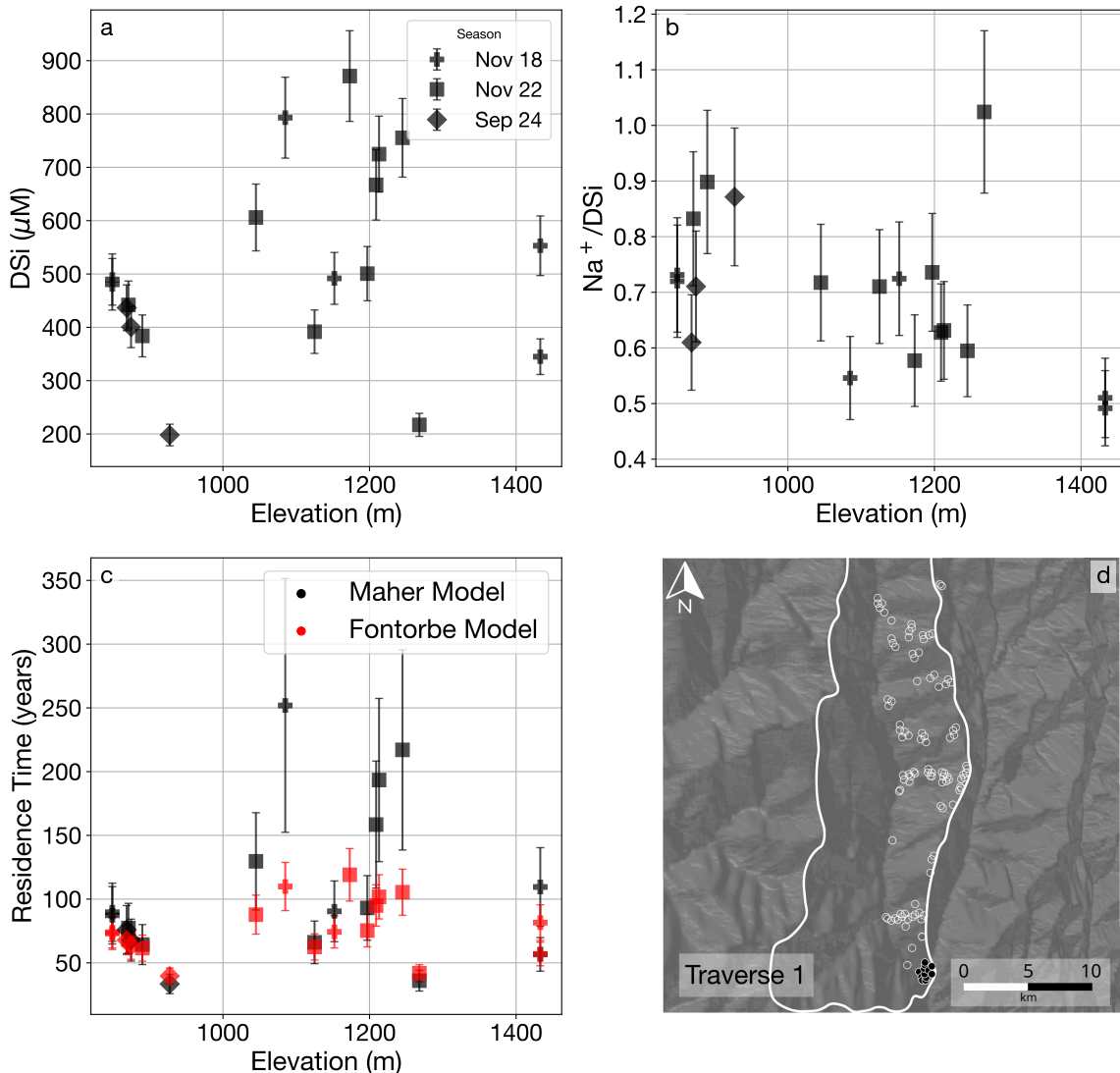


Figure 5: (a) DSi concentration against elevation for Traverse 1. Error bars reflect Monte Carlo error propagation. Different markers represent different seasons. (b)  $\text{Na}^+/\text{DSi}$  ratio against elevation. (c) Residence time estimates from the Fontorbe (red) and Maher model (black). (d) Spatial extent of Traverse 1 samples in the catchment. DEM data from NASA Space Systems (2018).

Concentration of DSi in the springs sampled in Traverse 1 is at a maximum for the whole catchment (see Figure 5). There is no clear trend of increasing DSi concentration but there is a potentially resolvable increase in  $\text{Na}^+/\text{DSi}$  with decreasing elevation. The Fontorbe

model predicts a peak of  $\approx 100$  years, while the Maher model predicts a much higher residence time of  $\approx 300$  years.

## 5.2 Traverse 2

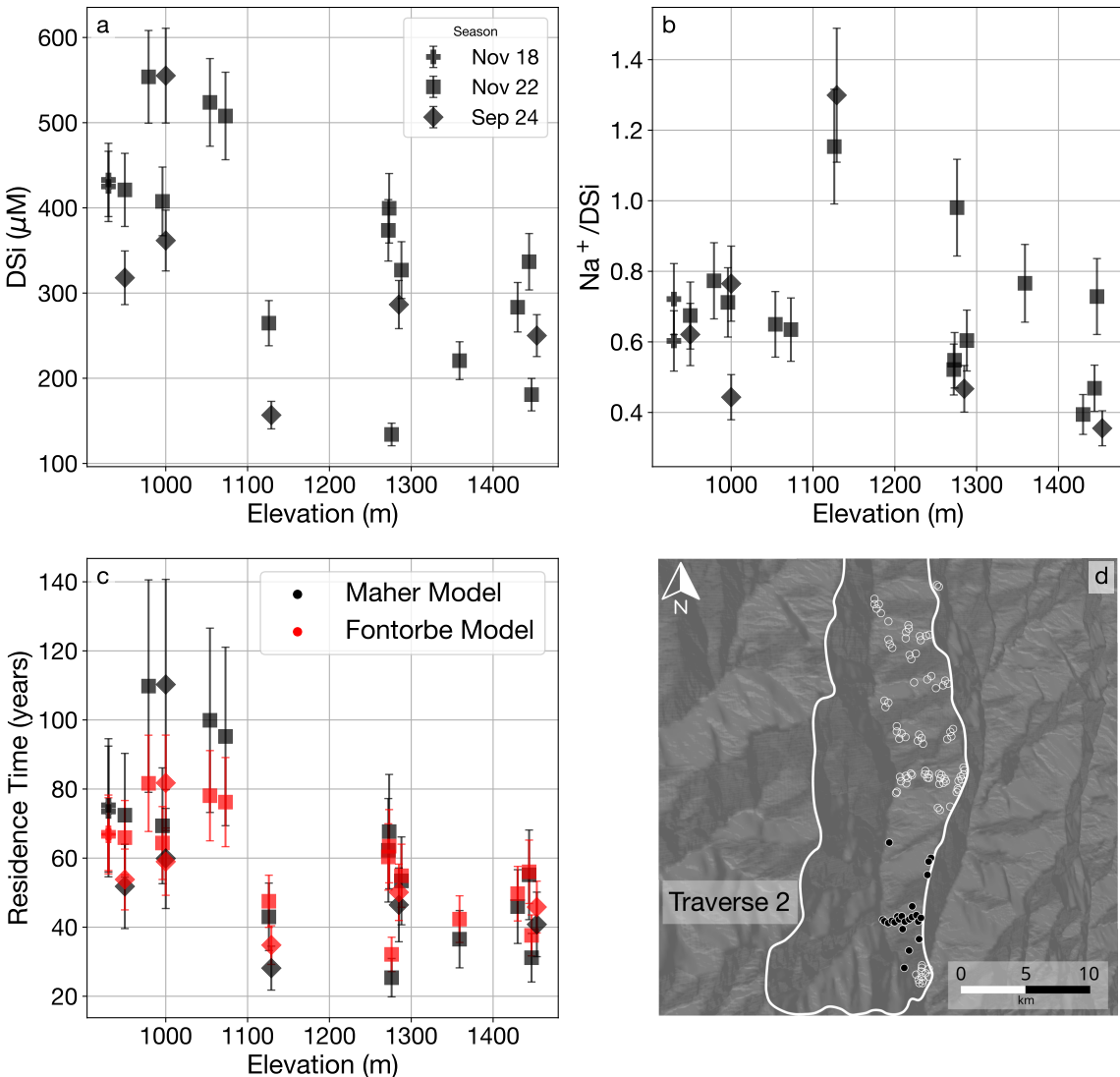


Figure 6: (a) DSi concentration against elevation for Traverse 2. Error bars reflect Monte Carlo error propagation. Different markers represent different seasons. (b)  $\text{Na}^+/\text{DSi}$  ratio against elevation. (c) Residence time estimates from the Fontorbe (red) and Maher model (black). (d) Spatial extent of Traverse 2 samples in the catchment. DEM data from NASA Space Systems (2018).

DSi shows a clear increase in concentration with decreasing elevation (see Figure 6). There is no resolvable trend with  $\text{Na}^+/\text{DSi}$  and elevation, nor with different seasons when

it was collected. Residence times are generally lower than those in Traverse 1, but both models showcase a clear trend of higher residence times at lower elevations. The Fontorbe model predicts generally older times than the Maher model at higher elevations, and younger times at lower elevations.

### 5.3 Traverse 3

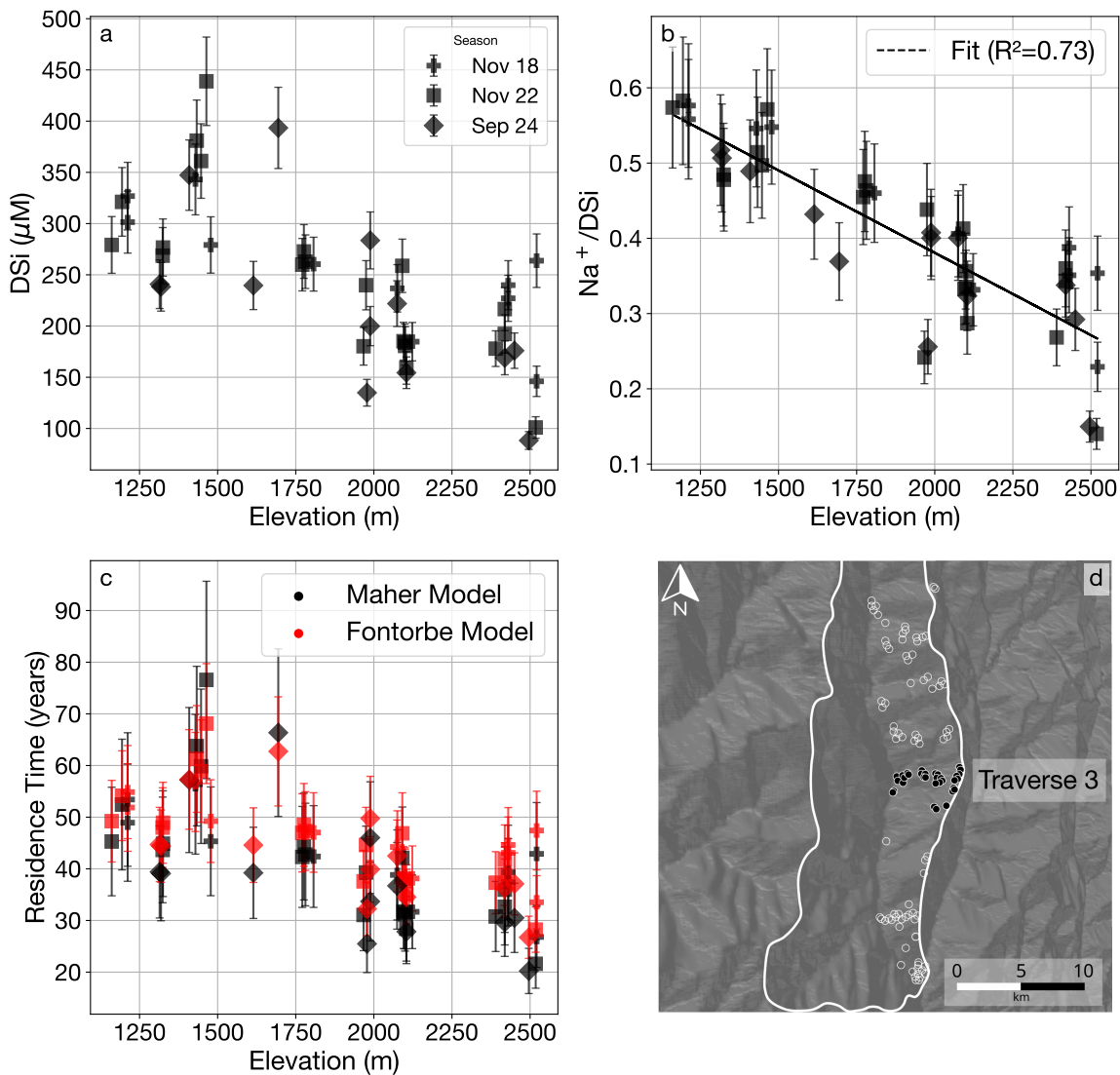
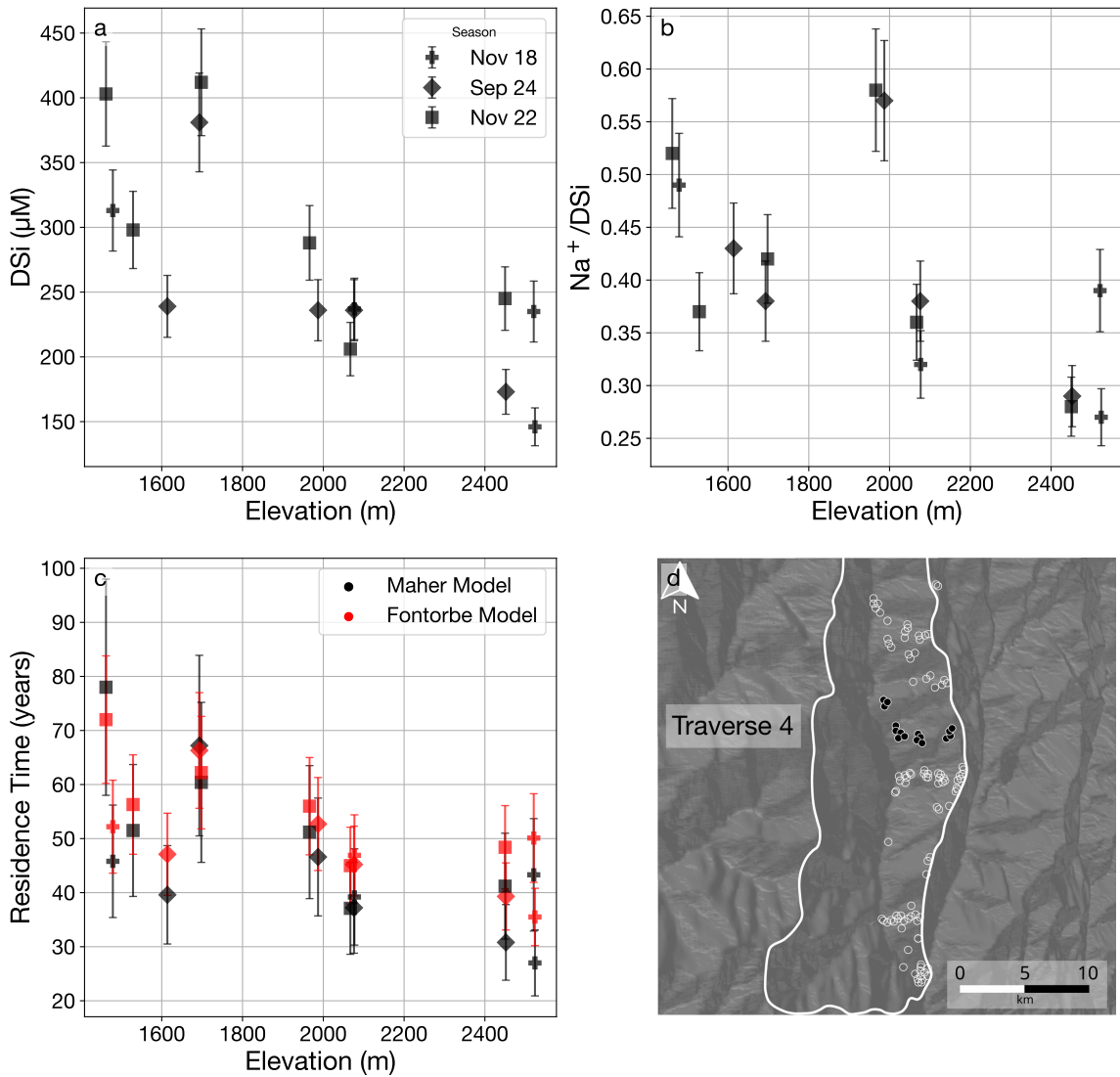


Figure 7: (a) Dissolved silica concentration against elevation for Traverse 3. Error bars reflect Monte Carlo error propagation. Different markers represent different seasons. (b)  $\text{Na}^+/\text{DSi}$  ratio against elevation. (c) Residence time estimates from the Fontorbe (red) and Maher model (black). (d) Spatial extent of Traverse 3 samples in the catchment. DEM data from NASA Space Systems (2018).

As elevation decreases, DSi concentration increases in Traverse 3 (see Figure 7). There is a potential dip at the lowermost elevation sampled.  $\text{Na}^+/\text{DSi}$  increases with decreasing elevation, consistent between different sampling seasons. Estimated residence times increase as elevation decreases, peaking at  $\approx 80$  years for the Maher model. This peak occurs at the same elevation as the highest DSi concentration.

## 5.4 Traverse 4

Traverse 4 is relatively undersampled compared to the other traverses (see Figure 8). DSi increases with decreasing elevation as seen in some of the previous traverses.  $\text{Na}^+/\text{DSi}$  generally increases with decreasing elevation. Residence times also increase with decreasing elevation as in the previous two traverses, with the Maher model predicting younger times at the highest elevations, and older times at the lowest elevations. The highest residence times predicted are  $\approx 80$  years.



**Figure 8:** (a) DSi concentration against elevation for Traverse 4. Error bars reflect Monte Carlo error propagation. Different markers represent different seasons. (b)  $\text{Na}^+/\text{DSi}$  ratio against elevation. (c) Residence time estimates from the Fontorbe (red) and Maher model (black). (d) Spatial extent of Traverse 4 samples in the catchment. DEM data from NASA Space Systems (2018).

## 5.5 Traverse 5

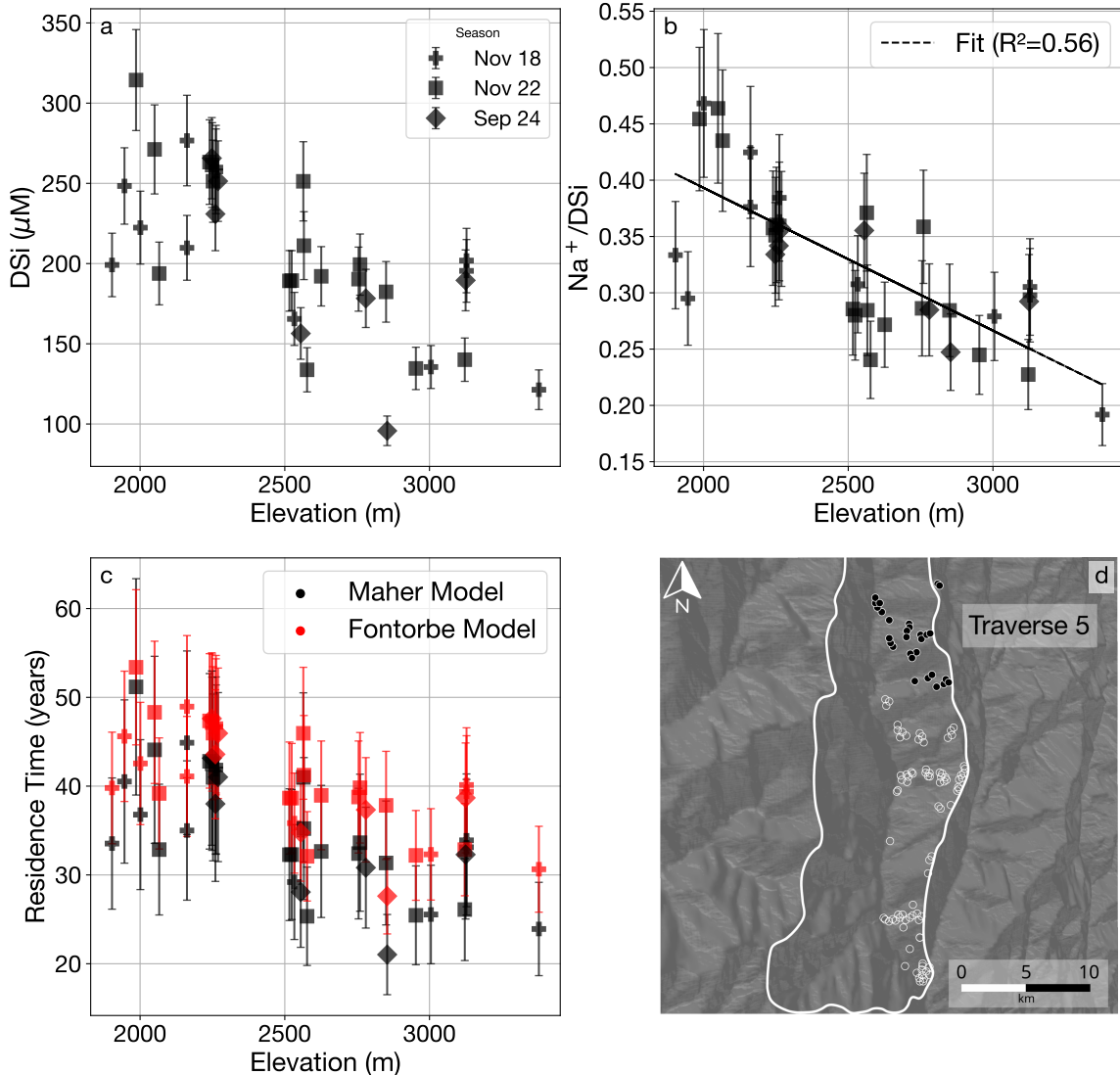


Figure 9: (a) DSi concentration against elevation for Traverse 5. Error bars reflect Monte Carlo error propagation. Different markers represent different seasons. (b)  $\text{Na}^+/\text{DSi}$  ratio against elevation. (c) Residence time estimates from the Fontorbe (red) and Maher model (black). (d) Spatial extent of Traverse 5 samples in the catchment. DEM data from NASA Space Systems (2018).

Traverse 5 is highly sampled and sits at the highest elevation of the whole catchment (see Figure 9). DSi concentration increases with decreasing elevation.  $\text{Na}^+/\text{DSi}$  similarly shows a trend of increasing ratio with decreasing elevation, and it is replicated between different seasons, with considerable scatter. Residence times increase with decreasing elevation, and are the lowest predicted in the catchments.

Table 4: Summary of results from each traverse. \* - All spring elemental concentrations are given after the rain and hydrothermal correction detailed in the Methods, aside from the chloride concentration. \*\* - Rain samples are displayed as measured, not corrected. Standard deviation of residence time corresponds to Monte Carlo propagated uncertainty

Spring Samples												
Sample ID	Season	Traverse	Elevation	Cl <sup>-</sup> *	DSi	Na <sup>+</sup>	K <sup>+</sup>	Ca <sup>2+</sup>	Sr <sup>2+</sup>	Na <sup>+</sup> /DSi	T <sub>Fontorbe</sub> ± 1 $\sigma$	T <sub>Maher</sub> ± 1 $\sigma$
				m		μM			nM			Years
NEP24-001	Sep 24	Traverse 1	928	93	207	184	6	86	875	0.89	41.9 ± 6.6	33.6 ± 7.6
NEP22-87	Nov 22	Traverse 1	1270	223	214	196	24	195	802	0.92	44.3 ± 7.0	36.2 ± 8.4
MKS 1B	Nov 18	Traverse 1	1432	25	295	180	11	22	250	0.61	60.3 ± 9.9	57.4 ± 14.0
NEP22-86	Nov 22	Traverse 1	1124	54	355	304	25	35	75	0.86	66.4 ± 10.8	67.5 ± 16.6
NEP22-2	Nov 22	Traverse 1	890	93	371	396	47	182	337	1.07	65.1 ± 10.4	65.4 ± 16.6
NEP22-1	Nov 22	Traverse 1	871	81	396	335	51	965	296	0.85	72.2 ± 12.0	78.4 ± 20.1
NEP22-85	Nov 22	Traverse 1	1195	2	446	411	19	87	192	0.92	79.7 ± 13.3	95.0 ± 25.1
NEP24-003	Sep 24	Traverse 1	876	86	446	289	68	179	246	0.65	67.2 ± 10.9	68.8 ± 17.0
NEP24-002	Sep 24	Traverse 1	868	100	456	295	60	832	252	0.65	71.9 ± 11.7	77.8 ± 20.2
MKS-3	Nov 18	Traverse 1	1152	7	478	341	48	96	590	0.71	78.7 ± 13.0	92.4 ± 23.9
MKS-24	Nov 18	Traverse 1	850	49	479	333	92	1085	463	0.7	77.2 ± 12.8	89.1 ± 23.6
MKS-1	Nov 18	Traverse 1	1433	37	583	343	20	99	544	0.59	86.4 ± 14.0	112.7 ± 30.0
NEP22-81	Nov 22	Traverse 1	1207	11	613	455	32	76	214	0.74	100.5 ± 16.4	164.9 ± 51.5
NEP22-80	Nov 22	Traverse 1	1046	6	666	472	31	83	267	0.71	92.3 ± 15.2	131.9 ± 38.6
NEP22-82	Nov 22	Traverse 1	1212	13	705	464	51	95	276	0.66	108.0 ± 17.8	206.2 ± 73.4
NEP22-83	Nov 22	Traverse 1	1244	4	766	407	50	130	327	0.53	111.5 ± 18.9	230.6 ± 94.8

Sample ID	Season	Traverse	Elevation	Cl <sup>-*</sup>	DSi	Na <sup>+</sup>	K <sup>+</sup>	Ca <sup>2+</sup>	Sr <sup>2+</sup>	Na <sup>+</sup> /DSi	T <sub>Fontorbe</sub> ± 1 $\sigma$	T <sub>Maher</sub> ± 1 $\sigma$
				m		μM		nM			Years	
MKS-2	Nov 18	Traverse 1	1083	8	821	417	55	124	258	0.51	116.6 ± 19.4	250.3 ± 118.4
NEP22-79	Nov 22	Traverse 2	1277	306	122	120	7	77	267	0.98	34.1 ± 5.3	25.6 ± 5.8
NEP22-63	Nov 22	Traverse 2	1447	152	190	136	11	16	498	0.72	39.9 ± 6.3	31.5 ± 7.0
NEP24-065	Sep 24	Traverse 2	1129	259	190	211	45	136	296	1.11	36.9 ± 5.7	28.4 ± 6.4
NEP22-66	Nov 22	Traverse 2	1359	126	241	160	11	3	31	0.66	45.0 ± 6.9	37.1 ± 8.5
NEP24-062	Sep 24	Traverse 2	1452	82	243	97	16	0	176	0.4	48.7 ± 7.7	41.4 ± 9.4
NEP22-65	Nov 22	Traverse 2	1429	59	267	122	16	2	137	0.46	52.8 ± 8.6	46.5 ± 10.5
NEP24-063	Sep 24	Traverse 2	1285	110	277	134	14	68	253	0.48	53.2 ± 8.7	47.1 ± 11.0
NEP24-067	Sep 24	Traverse 2	1000	58	298	295	39	102	377	0.99	62.6 ± 10.2	61.1 ± 14.9
NEP22-67	Nov 22	Traverse 2	1125	236	301	280	47	214	481	0.93	50.3 ± 8.1	43.5 ± 10.4
NEP24-068	Sep 24	Traverse 2	949	95	309	221	38	353	678	0.72	56.8 ± 9.3	52.2 ± 12.4
NEP22-68	Nov 22	Traverse 2	1288	113	311	239	13	85	230	0.77	58.2 ± 9.5	54.3 ± 13.2
MKS-10	Nov 18	Traverse 2	930	33	355	263	49	479	969	0.74	71.1 ± 11.7	76.3 ± 19.7
NEP22-71	Nov 22	Traverse 2	996	126	359	286	26	179	283	0.8	68.5 ± 11.2	71.3 ± 17.7
NEP22-64	Nov 22	Traverse 2	1442	102	371	171	17	28	366	0.46	59.5 ± 9.7	56.2 ± 13.6
NEP22-77	Nov 22	Traverse 2	1273	38	371	192	58	58	201	0.52	67.5 ± 11.2	69.4 ± 17.2
MKS10B	Nov 18	Traverse 2	929	36	386	384	55	511	1128	0.99	70.5 ± 11.6	75.0 ± 18.8
NEP22-78	Nov 22	Traverse 2	1270	40	393	188	24	32	184	0.48	63.7 ± 10.3	62.9 ± 15.3
NEP22-76	Nov 22	Traverse 2	1074	112	470	321	26	429	404	0.68	80.7 ± 13.4	97.9 ± 27.8
NEP22-70	Nov 22	Traverse 2	950	61	473	294	40	643	1250	0.62	70.0 ± 11.4	74.2 ± 18.6
NEP22-75	Nov 22	Traverse 2	1052	117	519	329	37	363	443	0.63	82.4 ± 13.7	101.5 ± 27.3

Sample ID	Season	Traverse	Elevation	Cl <sup>-*</sup>	DSi	Na <sup>+</sup>	K <sup>+</sup>	Ca <sup>2+</sup>	Sr <sup>2+</sup>	Na <sup>+</sup> /DSi	T <sub>Fontorbe</sub> ± 1 $\sigma$	T <sub>Maher</sub> ± 1 $\sigma$
											m	μM
NEP22-73	Nov 22	Traverse 2	979	42	639	456	68	224	837	0.71	82.6 ± 14.2	113.3 ± 31.0
NEP24-014	Sep 24	Traverse 3	2496	2	90	12	2	3	34	0.13	28.3 ± 4.3	20.3 ± 4.4
NEP22-9	Nov 22	Traverse 3	2522	2	99	11	2	5	42	0.11	29.9 ± 4.5	21.7 ± 4.7
NEP24-016	Sep 24	Traverse 3	1979	0	140	35	11	27	141	0.25	34.0 ± 5.3	25.5 ± 5.7
NEP24-015	Sep 24	Traverse 3	2101	7	160	61	8	0	200	0.38	36.6 ± 5.7	28.0 ± 6.2
NEP22-19	Nov 22	Traverse 3	2097	9	171	66	7	6	244	0.39	40.3 ± 6.3	31.8 ± 7.2
NEP22-13	Nov 22	Traverse 3	2098	9	172	71	8	6	249	0.41	40.1 ± 6.2	31.7 ± 7.2
NEP24-034	Sep 24	Traverse 3	2415	12	182	50	9	0	215	0.27	38.3 ± 6.2	29.8 ± 6.8
NEP22-46	Nov 22	Traverse 3	2555	3	183	65	11	61	159	0.36	37.3 ± 5.8	28.7 ± 6.5
NEP22-17	Nov 22	Traverse 3	2102	12	185	63	7	2	224	0.34	39.9 ± 6.2	31.5 ± 7.2
NEP22-20	Nov 22	Traverse 3	2104	7	186	53	7	0	113	0.28	37.0 ± 5.8	28.5 ± 6.4
NEP22-15	Nov 22	Traverse 3	1973	5	190	108	9	54	197	0.57	47.3 ± 7.7	39.7 ± 9.1
NEP22-12	Nov 22	Traverse 3	2386	3	192	42	3	15	153	0.22	39.4 ± 6.1	30.9 ± 7.0
MKS-6	Nov 18	Traverse 3	2124	9	195	65	8	0	160	0.33	40.2 ± 6.4	31.8 ± 7.2
NEP24-017	Sep 24	Traverse 3	1990	1	196	75	8	25	178	0.38	42.3 ± 6.6	34.0 ± 7.7
NEP22-11	Nov 22	Traverse 3	2418	16	197	90	6	2	206	0.46	44.3 ± 6.9	36.2 ± 8.1
NEP22-16	Nov 22	Traverse 3	1964	1	211	42	8	25	123	0.2	39.8 ± 6.2	31.3 ± 7.0
NEP22-10	Nov 22	Traverse 3	2418	17	217	64	5	0	194	0.29	41.6 ± 6.5	33.3 ± 7.5
MKS 5B	Nov 18	Traverse 3	2428	14	217	98	12	1	265	0.45	47.3 ± 7.5	39.7 ± 9.0
MKS-5	Nov 18	Traverse 3	2434	14	235	79	9	5	217	0.34	45.6 ± 7.2	37.8 ± 8.9
NEP24-011	Sep 24	Traverse 3	1318	11	239	112	14	32	334	0.47	47.0 ± 7.3	39.4 ± 9.0

Sample ID	Season	Traverse	Elevation	Cl <sup>-*</sup>	DSi	Na <sup>+</sup>	K <sup>+</sup>	Ca <sup>2+</sup>	Sr <sup>2+</sup>	Na <sup>+</sup> /DSi	T <sub>Fontorbe</sub> ± 1 $\sigma$	T <sub>Maher</sub> ± 1 $\sigma$
				m		μM		nM			Years	
NEP24-010	Sep 24	Traverse 3	1314	22	240	124	13	39	315	0.52	47.4 ± 7.6	39.8 ± 9.2
NEP22-55	Nov 22	Traverse 3	1772	20	251	119	17	33	319	0.47	49.9 ± 7.9	42.9 ± 10.1
MKS-7	Nov 18	Traverse 3	1805	21	257	104	19	32	300	0.4	50.0 ± 8.1	43.0 ± 10.1
NEP22-42	Nov 22	Traverse 3	1325	27	258	137	9	35	351	0.53	51.8 ± 8.4	45.4 ± 10.7
NEP22-58	Nov 22	Traverse 3	1447	8	271	166	14	74	326	0.61	62.2 ± 10.4	60.4 ± 14.5
NEP22-60	Nov 22	Traverse 3	1160	23	279	184	19	63	323	0.66	52.3 ± 8.4	46.0 ± 10.3
NEP22-18	Nov 22	Traverse 3	2091	9	281	101	15	25	362	0.36	49.7 ± 7.9	42.7 ± 9.8
NEP22-53	Nov 22	Traverse 3	1777	20	284	113	17	46	392	0.4	51.3 ± 8.4	44.8 ± 10.6
NEP22-59	Nov 22	Traverse 3	1324	15	291	134	12	30	351	0.46	50.9 ± 8.2	44.2 ± 10.2
NEP22-54	Nov 22	Traverse 3	1779	20	294	112	15	38	387	0.38	50.1 ± 8.0	43.2 ± 10.0
NEP22-45	Nov 22	Traverse 3	1195	24	315	184	6	47	323	0.58	57.6 ± 9.1	53.4 ± 12.6
MKS 9B	Nov 18	Traverse 3	1214	16	349	192	10	44	384	0.55	58.5 ± 9.7	54.6 ± 12.9
MKS-9	Nov 18	Traverse 3	1212	17	354	193	11	47	311	0.55	54.8 ± 8.7	49.4 ± 11.6
NEP22-56	Nov 22	Traverse 3	1433	23	356	209	13	83	401	0.59	68.0 ± 11.9	77.3 ± 17.0
NEP24-038	Sep 24	Traverse 3	1408	20	369	155	19	69	406	0.42	60.6 ± 10.0	58.0 ± 14.3
MKS-8	Nov 18	Traverse 3	1430	15	431	190	17	72	408	0.44	60.3 ± 10.0	57.5 ± 14.0
MKS 4B	Nov 18	Traverse 4	2524	3	146	39	2	1	108	0.27	35.5 ± 5.3	27.0 ± 6.1
NEP24-050	Sep 24	Traverse 4	2452	2	173	51	7	11	141	0.29	39.3 ± 6.2	30.8 ± 7.0
NEP22-48	Nov 22	Traverse 4	2067	3	206	75	7	32	254	0.36	45.0 ± 7.1	37.1 ± 8.5
MKS-4	Nov 18	Traverse 4	2521	2	235	92	9	31	207	0.39	50.1 ± 8.2	43.3 ± 10.4
NEP24-052	Sep 24	Traverse 4	1987	0	236	134	17	73	382	0.57	52.7 ± 8.6	46.6 ± 10.9

Sample ID	Season	Traverse	Elevation	Cl <sup>-*</sup>	DSi	Na <sup>+</sup>	K <sup>+</sup>	Ca <sup>2+</sup>	Sr <sup>2+</sup>	Na <sup>+</sup> /DSi	T <sub>Fontorbe</sub> ± 1 $\sigma$	T <sub>Maher</sub> ± 1 $\sigma$
				m		μM		nM			Years	
NEP24-051	Sep 24	Traverse 4	2076	2	236	89	10	25	212	0.38	45.2 ± 7.1	37.2 ± 8.4
MKS-13	Nov 18	Traverse 4	2077	2	237	77	9	31	236	0.32	46.9 ± 7.5	39.2 ± 8.9
NEP24-041	Sep 24	Traverse 4	1614	12	239	103	25	17	246	0.43	47.1 ± 7.6	39.6 ± 9.1
NEP22-47	Nov 22	Traverse 4	2450	8	245	68	7	31	169	0.28	48.4 ± 7.7	41.2 ± 9.8
NEP22-49	Nov 22	Traverse 4	1966	5	288	167	13	61	424	0.58	56.0 ± 9.0	51.2 ± 12.3
NEP22-52	Nov 22	Traverse 4	1529	8	298	111	7	20	158	0.37	56.3 ± 9.2	51.5 ± 12.2
MKS-12	Nov 18	Traverse 4	1479	9	313	153	29	100	408	0.49	52.2 ± 8.6	45.8 ± 10.4
NEP24-040	Sep 24	Traverse 4	1693	22	381	145	12	86	590	0.38	66.3 ± 10.7	67.2 ± 16.7
NEP22-57	Nov 22	Traverse 4	1462	46	403	211	21	104	661	0.52	72.0 ± 11.8	78.0 ± 20.0
NEP22-50	Nov 22	Traverse 4	1698	21	412	173	22	73	682	0.42	62.2 ± 10.4	60.4 ± 14.8
NEP24-027	Sep 24	Traverse 5	2858	2	105	25	10	11	68	0.24	29.2 ± 4.4	21.1 ± 4.6
NEP22-28	Nov 22	Traverse 5	2954	2	107	30	8	17	92	0.28	34.1 ± 5.2	25.6 ± 5.7
MKS-23	Nov 18	Traverse 5	3379	1	124	21	0	5	47	0.17	32.6 ± 5.0	24.2 ± 5.4
MKS 21B	Nov 18	Traverse 5	3007	4	144	35	9	1	29	0.24	34.3 ± 5.3	25.8 ± 5.7
NEP24-020	Sep 24	Traverse 5	2556	4	150	59	13	26	216	0.39	37.0 ± 5.8	28.5 ± 6.5
NEP22-39	Nov 22	Traverse 5	2523	5	165	53	13	37	182	0.32	41.0 ± 6.6	32.6 ± 7.4
NEP24-028	Sep 24	Traverse 5	2782	2	167	54	17	24	169	0.32	39.4 ± 6.2	30.9 ± 7.0
MKS-14	Nov 18	Traverse 5	2536	2	172	51	13	24	143	0.3	37.9 ± 5.9	29.4 ± 6.7
NEP22-27	Nov 22	Traverse 5	3126	2	172	40	10	12	81	0.23	34.9 ± 5.4	26.4 ± 5.9
NEP22-23	Nov 22	Traverse 5	2517	1	173	56	8	21	115	0.32	40.8 ± 6.5	32.4 ± 7.4
NEP22-26	Nov 22	Traverse 5	2579	2	176	31	9	16	110	0.18	34.1 ± 5.2	25.6 ± 5.7

Sample ID	Season	Traverse	Elevation	Cl <sup>-*</sup>	DSi	Na <sup>+</sup>	K <sup>+</sup>	Ca <sup>2+</sup>	Sr <sup>2+</sup>	Na <sup>+</sup> /DSi	T <sub>Fontorbe</sub> ± 1 $\sigma$	T <sub>Maher</sub> ± 1 $\sigma$
				m	μM	nM				Years		
MKS-22	Nov 18	Traverse 5	3126	2	179	62	15	30	207	0.35	42.3 ± 6.6	34.1 ± 7.8
NEP24-022	Sep 24	Traverse 5	2259	12	187	72	11	25	179	0.39	46.0 ± 7.2	38.2 ± 8.7
NEP24-025	Sep 24	Traverse 5	3127	0	190	57	16	31	202	0.3	40.9 ± 6.4	32.5 ± 7.3
NEP22-35	Nov 22	Traverse 5	2068	3	198	94	19	94	152	0.47	41.5 ± 6.5	33.1 ± 7.5
NEP22-24	Nov 22	Traverse 5	2622	6	198	48	16	46	203	0.24	41.2 ± 6.6	32.8 ± 7.4
NEP22-22	Nov 22	Traverse 5	2758	2	205	55	18	44	192	0.27	41.2 ± 6.5	32.8 ± 7.5
MKS 22B	Nov 18	Traverse 5	3130	2	211	53	16	34	183	0.25	41.8 ± 6.6	33.5 ± 7.7
NEP22-29	Nov 22	Traverse 5	2852	2	215	54	12	23	124	0.25	40.3 ± 6.3	31.9 ± 7.3
NEP22-30	Nov 22	Traverse 5	2757	3	217	56	20	50	196	0.26	42.2 ± 6.6	33.9 ± 7.8
MKS-17	Nov 18	Traverse 5	2163	2	218	87	16	62	60	0.4	43.4 ± 6.8	35.2 ± 8.0
NEP22-25	Nov 22	Traverse 5	2562	4	227	63	17	49	273	0.28	43.8 ± 6.8	35.7 ± 8.1
MKS-20	Nov 18	Traverse 5	1903	9	227	60	0	9	163	0.26	42.1 ± 6.7	33.8 ± 7.7
NEP22-31	Nov 22	Traverse 5	2573	2	228	98	20	56	282	0.43	48.6 ± 7.6	41.4 ± 9.3
NEP24-023	Sep 24	Traverse 5	2269	15	239	97	20	41	281	0.41	48.8 ± 7.8	41.6 ± 9.8
NEP22-33	Nov 22	Traverse 5	2247	13	239	92	15	44	303	0.38	50.0 ± 8.0	43.1 ± 10.2
MKS 15B	Nov 18	Traverse 5	2000	11	248	95	33	59	244	0.38	45.2 ± 7.2	37.3 ± 8.5
MKS-18	Nov 18	Traverse 5	2262	10	248	89	23	35	227	0.36	49.5 ± 8.0	42.4 ± 9.9
MKS-16	Nov 18	Traverse 5	1942	10	251	70	28	258	413	0.28	48.2 ± 7.7	40.9 ± 9.3
MKS 18B	Nov 18	Traverse 5	2265	13	261	113	18	36	226	0.43	49.8 ± 8.0	42.8 ± 9.9
NEP22-32	Nov 22	Traverse 5	2252	11	267	91	19	44	260	0.34	48.6 ± 7.7	41.4 ± 9.9
MKS-19	Nov 18	Traverse 5	2164	14	276	100	5	32	307	0.36	51.6 ± 8.3	45.1 ± 10.5

Sample ID	Season	Traverse	Elevation	Cl <sup>-*</sup>	DSi	Na <sup>+</sup>	K <sup>+</sup>	Ca <sup>2+</sup>	Sr <sup>2+</sup>	Na <sup>+</sup> /DSi	T <sub>Fontorbe</sub> ± 1 $\sigma$	T <sub>Maher</sub> ± 1 $\sigma$
				m		μM		nM			Years	
NEP22-37	Nov 22	Traverse 5	2050	2	276	130	20	114	207	0.47	51.4 ± 8.3	44.8 ± 10.3
NEP24-021	Sep 24	Traverse 5	2243	20	278	96	21	35	259	0.35	50.1 ± 8.0	43.3 ± 10.1
NEP22-34	Nov 22	Traverse 5	2240	17	312	91	16	47	264	0.29	50.1 ± 8.4	43.2 ± 10.4
NEP22-36	Nov 22	Traverse 5	1987	3	352	156	22	117	271	0.44	56.6 ± 9.0	52.0 ± 12.6
<b>Rain Samples</b>												
Sample ID	Season	Traverse	Elevation	Cl <sup>-**</sup>	DSi**	Na <sup>++**</sup>	K <sup>++**</sup>	Ca <sup>2+**</sup>	Sr <sup>2+**</sup>	Na <sup>+</sup> /DSi**		
				m		nM						
NEP24-039	Sep 24	Traverse 1	840	28085	163752	90995	15181	108552	128	1		
NEP24-012	Sep 24	Traverse 2	1950	1369	90	3708	1742	8372	4	41		
NEP24-044	Sep 24	Traverse 2	1952	1887	138	5769	2796	11849	8	42		
NEP24-036	Sep 24	Traverse 2	1952	7333	311	2003	1353	10383	5	6		
NEP24-030	Sep 24	Traverse 2	1950	565	629	2174	1420	18259	10	3		
NEP24-058	Sep 24	Traverse 2	1950	809	2024	2297	1365	13619	9	1		
NEP24-045	Sep 24	Traverse 3	2644	3213	52	2213	1202	4289	8	43		
NEP24-047	Sep 24	Traverse 3	2644	548	431	3378	4850	9949	10	8		
NEP24-057	Sep 24	Traverse 3	2110	5840	955	2892	1023	27033	15	3		
NEP24-046	Sep 24	Traverse 3	2110	2858	1092	4904	1851	26459	18	4		
NEP24-035	Sep 24	Traverse 3	2110	1343	1392	4329	1486	33703	24	3		
NEP24-055	Sep 24	Traverse 3	2644	257	1456	5054	7475	24931	16	3		
NEP24-059	Sep 24	Traverse 3	1366	32021	1938	2669	7508	47975	38	1		
NEP24-054	Sep 24	Traverse 3	2110	6508	2436	4978	2132	38633	25	2		

## Time Series Trends

Concentrations of DSi in several springs in the catchment show a consistent decrease in concentration with the onset of the monsoon (see Figure 10). Concentrations are high in April, decrease to a minimum in September, then slowly increase back to April levels through October and November. Decrease in concentration is likely a sign of dilution from increased precipitation during the monsoon. Such a trend is also present in a time series of a spring in Traverse 3. The average April-September decrease is small compared to the average DSi concentration of the rain.

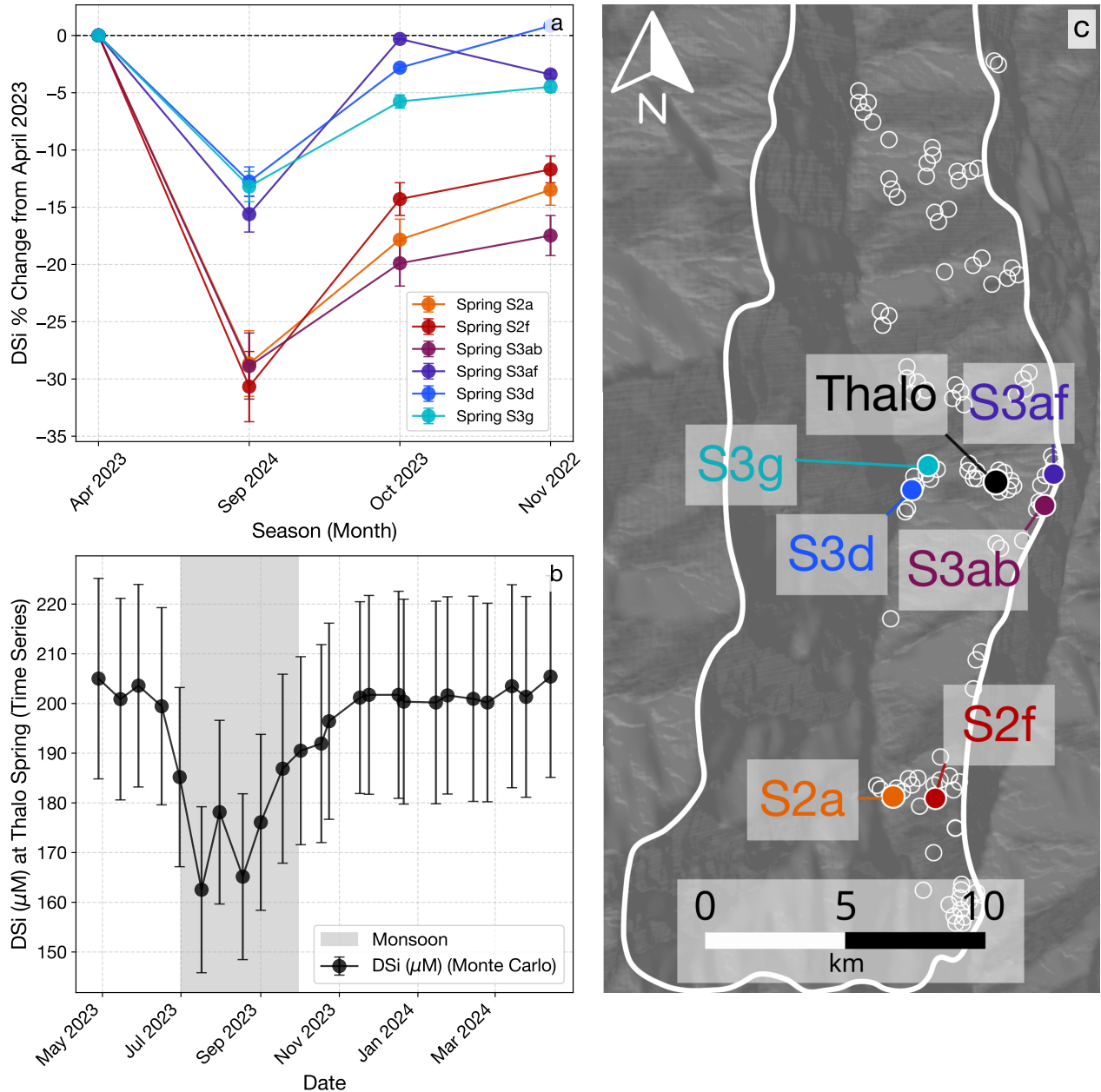


**Figure 10:** (a) Measured spring silica concentrations against season sampled. Note that in order to show different seasons, the values plotted are uncorrected. This is because for the April and October 2023 seasons, no chloride concentration was measured, so no correction was carried out. DSi is represented as a percentage change from April 2023, to emphasise monsoonal dilution. (b) Dissolved Silica against date sampled for time series sampled collected at a single spring, Thalo. Error bars represent monte carlo error propagation. (c) Schematic of the Melamchi catchment showing the location of springs plotted in (a) and (b).

## 6 Discussion

### 6.1 Explaining Traversal Variations in Chemistry

Increasing DSi concentration with decreasing elevation suggests the springs are sampling increasingly longer flow paths. This is because longer flow paths allow for more water-rock interaction, which scavenges more DSi from the silicate rocks. While most traverses show such a trend, this does not happen in Traverse 1. One possible reason is that the lowermost springs are likely to be close to the Melamchi river; this is more dilute than the most concentrated springs in the traverse. Mixing with the river waters is possible but unlikely because of the difference in elevation. It is unlikely that the decrease is caused by a dilution effect at the start of the monsoon such as that shown in Figure 10. This is because these DSi trends are consistent across multiple seasons within error. Clearly, however, samples collected in September will be relatively more dilute than those collected in April.

A decrease in DSi at lower elevations here could also suggest precipitation of secondary minerals, which is apparent from the  $\text{Na}^+/\text{DSi}$  ratio. Linear trends in plot (b) for Traverses 1, 3, and 5 show an increase in  $\text{Na}^+/\text{DSi}$  as elevation decreases. Elevated  $\text{Na}^+/\text{DSi}$  is interpreted as a sign of a closer approach to equilibrium. Si is involved in kaolinite precipitation whilst  $\text{Na}^+$  is not, as evidenced in equation 4, so an increase in their ratio suggests more kaolinite is precipitating (Gaillardet et al., 1999). Kaolinite precipitation is considered to be the backwards reaction, so its increase points to an approach towards equilibrium.

Plots of  $\text{Na}^+/\text{DSi}$  against elevation can also be used to infer how consistently a given flow path is sampled. Because  $\text{Na}^+/\text{DSi}$  is primarily controlled by the balance of dissolution and reprecipitation, and by extension the average age of water in the flow path, consistency of this value over time points to the same flow path length being sampled for a given rate of reaction. Under the steady state assumption assumption  $\partial C / \partial t = 0$  used in the residence time models, the  $\text{Na}/\text{DSi}$  ratio should be constant over time at a given elevation if the same flow path is sampled (Lichtner, 1988). For both Traverse 3 and 5, the  $\text{Na}^+/\text{DSi}$  ratio

against elevation does not change between different seasons. However, there is a better correlation in Traverse 3 which suggests that the flow paths are more consistently sampled there.

## 6.2 Residence Time Agreement with Gas Ages

As shown in Figures 5-9 (c), predicted residence times in the catchment are consistent between the Maher and Fontorbe Models. Residence times increase as elevation decreases, agreeing with the notion that springs sampled at these lower elevations reflect longer flow-paths. Residence times also generally increase with decreasing traversal number, such that Traverse 5 has the lowest and Traverse 1 has the highest. Consistently increasing residence times like this could suggest catchment-wide plumbing, whereby traversal flow paths are interconnected.

Residence times in Traverse 3 can be directly compared to the gas ages obtained by Atwood (2023), because both studies are sampling the same springs. The Atwood (2023) ages in Traverse 3 range from 5-35 years. The findings from this study and both models predict residence times of a similar order of magnitude. This study does predict older times at the lowest elevation, but these are mostly within the range of propagated uncertainty. Using spring chemistry is therefore a viable method to determine residence times in natural catchments, with the premise that the model assumptions are valid. In addition, this study lends credibility to the use of gas ages to determine residence times, which is an approach that is often criticised for using biased age distributions (McCallum et al., 2015). Findings of residence times on the order of 10-100 years for the whole catchment also inform precipitation-discharge relationships. If this study's findings are correct, then the delay in river discharge found by Andermann et al. (2012) is likely only recording surface or near-surface flow. The shorter flow paths here could plausibly be associated to residence times of a few months.

The fact that both the kinetic-dependent rate Maher model and the kinetics-independent

rate Fontorbe model agree with Atwood (2023) suggests that the groundwater in Traverse 3 does not get near equilibrium. Reaction rate is kept constant in the Fontorbe model assuming a far from equilibrium state. In the Maher model, reaction rate depends on the equilibrium concentration. As this concentration is reached in the Maher model, the reaction rate will decrease. When the system is far from equilibrium, both models will predict similar times. In order to do test this further, the free energy of the system can be calculated.

### 6.3 Free Energy Calculations Concur on Far From Equilibrium State

Maher (2011) uses their model to conclude that all flow paths reach equilibrium. The free energy of reaction, calculated using the activity of the ions in solution, can be used in natural systems to determine the extent to which equilibrium is reached (Kampman et al., 2009; Wojtowicz, 2001). Free energies lower than -10 kJ/mol are considered close to equilibrium, whilst those more negative than -40 kJ/mol are categorised as far from equilibrium (Kampman et al., 2009). This method can therefore test the validity of the Maher model in Melamchi. Free energy is defined as:

$$\Delta G = \Delta G^0 + RT \ln Q \quad (13)$$

Where in equation 13,  $\Delta G$  represents the Gibbs free energy change of reaction,  $\Delta G^0$  is the standard Gibbs free energy change,  $R$  is the universal gas constant,  $T$  denotes the absolute temperature in kelvins, and  $Q$  is the reaction quotient. As discussed in the Methods 4.2, the weathering reaction characterising this catchment is the dissolution of plagioclase (An-20) and the precipitation of kaolinite, given by equation 4. The exact composition of plagioclase is important for these calculations. The free energy of reaction is lowered by the presence of a solid solution between albite and anorthite (Dubacq, 2022). The parameters for the standard free energy of reaction are calculated using the pygcc python package (Awolayo & Tutolo, 2022). The package gives the standard properties of solid-solution

species and reactions, such that  $\Delta G^0$  can be calculated:

$$\Delta G^0 = \Delta G_{products}^0 - \Delta G_{reactants}^0 = -RT \ln K \quad (14)$$

$K$  is calculated using the database obtained from pygcc using The Geochemist's Workbench® Rxn program (Bethke, 2011).  $Q$  is calculated as the ion activity product of the reaction, assuming the activities of the solid phases plagioclase and kaolinite are 1, the activity of water is 1, and the activity of the ions in solution are equal to their concentration.

$$Q = \frac{a_{\text{Kaol}}^{0.6} a_{\text{Na}^+}^{0.8} a_{\text{Ca}^{2+}}^{0.2} a_{\text{SiO}_2(\text{aq})}^{1.6}}{a_{\text{An}_{20}}^{1.2} a_{\text{H}^+}^{1.2}} \quad (15)$$

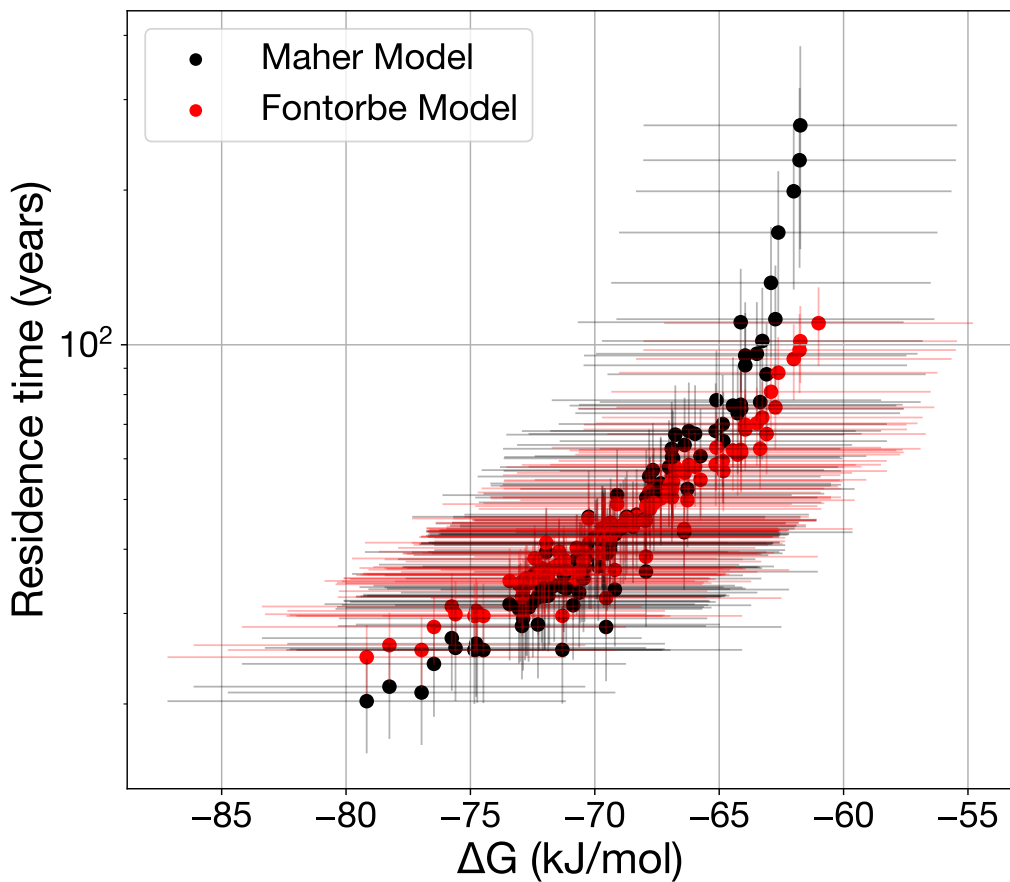


Figure 11: Estimated residence time against calculated free energy of reaction. Error bars represent Monte Carlo propagated uncertainty. Red points plot the Fontorbe model, while black points plot the Maher model.

Figure 11 shows that all springs in the catchment have a free energy that is more nega-

tive than -60 kJ/mol. These samples are therefore classified as far from equilibrium. Note that being far from equilibrium is not inconsistent with evidence for secondary precipitation as shown in Figures 3, 5-9; simply, being closer to equilibrium would suggest more precipitation. Figure 11 does show that free energy gets closer to zero as residence time increases. This is consistent with the notion that groundwaters approach equilibrium the more they stay in the subsurface and react. However, the extent of reaction is not great enough to be considered close to equilibrium. This suggests that, for Melamchi, using the Maher model to estimate residence times is not appropriate.

Table 5: Summary of free energy results from each traverse. Standard deviation corresponds to Monte Carlo propagated uncertainty.

Sample ID	Season	Traverse	Elevation	$\Delta G \pm 1\sigma$	Sample ID	Season	Traverse	Elevation	$\Delta G \pm 1\sigma$	Sample ID	Season	Traverse	Elevation	$\Delta G \pm 1\sigma$
			m	kJ/mol				m	kJ/mol				m	kJ/mol
NEP24-001	Sep 24	Traverse 1	928	-69.7 ± 7.1	NEP22-65	Nov 22	Traverse 2	1429	-70.8 ± 7.2	NEP22-17	Nov 22	Traverse 3	2102	-74.0 ± 7.5
NEP22-87	Nov 22	Traverse 1	1270	-68.5 ± 7.0	NEP24-065	Sep 24	Traverse 2	1129	-70.1 ± 7.1	NEP22-12	Nov 22	Traverse 3	2386	-73.6 ± 7.5
MKS1B	Nov 18	Traverse 1	1432	-68.2 ± 7.0	NEP24-063	Sep 24	Traverse 2	1285	-68.8 ± 7.0	NEP22-16	Nov 22	Traverse 3	1964	-73.4 ± 7.5
NEP22-86	Nov 22	Traverse 1	1124	-66.5 ± 6.8	NEP22-64	Nov 22	Traverse 2	1442	-68.3 ± 7.0	NEP22-19	Nov 22	Traverse 3	2097	-73.4 ± 7.5
NEP24-003	Sep 24	Traverse 1	876	-65.6 ± 6.7	NEP22-78	Nov 22	Traverse 2	1270	-67.5 ± 6.9	NEP22-13	Nov 22	Traverse 3	2098	-73.2 ± 7.5
NEP22-2	Nov 22	Traverse 1	890	-65.3 ± 6.7	NEP22-68	Nov 22	Traverse 2	1288	-67.4 ± 6.9	NEP22-10	Nov 22	Traverse 3	2418	-73.1 ± 7.4
MKS-1	Nov 18	Traverse 1	1433	-64.6 ± 6.6	NEP22-67	Nov 22	Traverse 2	1125	-66.9 ± 6.8	NEP22-11	Nov 22	Traverse 3	2418	-73.0 ± 7.4
NEP24-002	Sep 24	Traverse 1	868	-64.6 ± 6.6	NEP24-068	Sep 24	Traverse 2	949	-66.9 ± 6.8	NEP22-46	Nov 22	Traverse 3	2555	-72.8 ± 7.4
NEP22-85	Nov 22	Traverse 1	1195	-64.5 ± 6.6	NEP22-77	Nov 22	Traverse 2	1273	-66.7 ± 6.8	MKS 5B	Nov 18	Traverse 3	2428	-72.5 ± 7.4
MKS-3	Nov 18	Traverse 1	1152	-64.4 ± 6.6	NEP24-067	Sep 24	Traverse 2	1000	-66.2 ± 6.8	MKS-5	Nov 18	Traverse 3	2434	-72.0 ± 7.3
NEP22-1	Nov 22	Traverse 1	871	-63.8 ± 6.5	NEP22-71	Nov 22	Traverse 2	996	-65.3 ± 6.7	NEP24-017	Sep 24	Traverse 3	1990	-71.8 ± 7.3
MKS-24	Nov 18	Traverse 1	850	-63.6 ± 6.5	MKS-10	Nov 18	Traverse 2	930	-65.0 ± 6.7	NEP22-15	Nov 22	Traverse 3	1973	-70.2 ± 7.2
NEP22-80	Nov 22	Traverse 1	1046	-63.4 ± 6.5	NEP22-70	Nov 22	Traverse 2	950	-64.8 ± 6.6	NEP22-18	Nov 22	Traverse 3	2091	-70.2 ± 7.2
NEP22-81	Nov 22	Traverse 1	1207	-63.1 ± 6.4	MKS 10B	Nov 18	Traverse 2	929	-64.6 ± 6.6	NEP24-011	Sep 24	Traverse 3	1318	-70.1 ± 7.1
NEP22-82	Nov 22	Traverse 1	1212	-62.5 ± 6.4	NEP22-76	Nov 22	Traverse 2	1074	-64.0 ± 6.6	NEP24-010	Sep 24	Traverse 3	1314	-70.0 ± 7.1
NEP22-83	Nov 22	Traverse 1	1244	-62.3 ± 6.4	NEP22-75	Nov 22	Traverse 2	1052	-63.8 ± 6.5	MKS-7	Nov 18	Traverse 3	1805	-69.8 ± 7.1
MKS-2	Nov 18	Traverse 1	1083	-62.2 ± 6.4	NEP22-73	Nov 22	Traverse 2	979	-63.2 ± 6.5	NEP22-55	Nov 22	Traverse 3	1772	-69.8 ± 7.1
NEP24-061	Sep 24	Traverse 2	1527	-76.4 ± 7.8	NEP24-014	Sep 24	Traverse 3	2496	-79.8 ± 8.1	NEP22-54	Nov 22	Traverse 3	1779	-69.7 ± 7.1
NEP22-61	Nov 22	Traverse 2	1524	-76.3 ± 7.7	NEP22-9	Nov 22	Traverse 3	2522	-78.9 ± 8.0	NEP22-59	Nov 22	Traverse 3	1324	-69.5 ± 7.1
NEP24-062	Sep 24	Traverse 2	1452	-72.5 ± 7.4	NEP24-015	Sep 24	Traverse 3	2101	-75.1 ± 7.6	NEP22-53	Nov 22	Traverse 3	1777	-69.4 ± 7.0
NEP22-62	Nov 22	Traverse 2	1504	-71.8 ± 7.3	NEP24-016	Sep 24	Traverse 3	1979	-75.0 ± 7.7	NEP22-42	Nov 22	Traverse 3	1325	-69.3 ± 7.1
NEP22-79	Nov 22	Traverse 2	1277	-71.8 ± 7.3	NEP24-034	Sep 24	Traverse 3	2415	-74.9 ± 7.6	NEP22-60	Nov 22	Traverse 3	1160	-68.5 ± 7.0
NEP22-63	Nov 22	Traverse 2	1447	-71.4 ± 7.3	MKS-6	Nov 18	Traverse 3	2124	-74.6 ± 7.6	MKS-9	Nov 18	Traverse 3	1212	-68.4 ± 7.0
NEP22-66	Nov 22	Traverse 2	1359	-71.0 ± 7.2	NEP22-20	Nov 22	Traverse 3	2104	-74.6 ± 7.6	MKS 9B	Nov 18	Traverse 3	1214	-67.8 ± 6.9

Sample ID	Season	Traverse	Elevation	$\Delta G \pm 1\sigma$
			m	kJ/mol
NEP22-45	Nov 22	Traverse 3	1195	-67.8 ± 6.9
NEP24-038	Sep 24	Traverse 3	1408	-67.6 ± 6.9
MKS-8	Nov 18	Traverse 3	1430	-67.4 ± 6.9
NEP22-58	Nov 22	Traverse 3	1447	-67.4 ± 6.9
NEP22-56	Nov 22	Traverse 3	1433	-66.9 ± 6.8
MKS 4B	Nov 18	Traverse 4	2524	-76.3 ± 7.8
NEP24-050	Sep 24	Traverse 4	2452	-73.6 ± 7.5
NEP22-48	Nov 22	Traverse 4	2067	-71.1 ± 7.2
NEP24-051	Sep 24	Traverse 4	2076	-71.0 ± 7.3
NEP24-041	Sep 24	Traverse 4	1614	-70.8 ± 7.2
MKS-13	Nov 18	Traverse 4	2077	-70.7 ± 7.2
NEP22-47	Nov 22	Traverse 4	2450	-70.5 ± 7.2
MKS-4	Nov 18	Traverse 4	2521	-70.3 ± 7.2
NEP22-52	Nov 22	Traverse 4	1529	-69.6 ± 7.1
NEP24-052	Sep 24	Traverse 4	1987	-69.2 ± 7.1
MKS-12	Nov 18	Traverse 4	1479	-68.5 ± 7.0
NEP22-49	Nov 22	Traverse 4	1966	-68.5 ± 7.0
NEP22-50	Nov 22	Traverse 4	1698	-67.4 ± 6.9
NEP24-040	Sep 24	Traverse 4	1693	-67.3 ± 6.9
NEP22-57	Nov 22	Traverse 4	1462	-65.6 ± 6.7
NEP24-027	Sep 24	Traverse 5	2858	-77.6 ± 7.9
MKS-23	Nov 18	Traverse 5	3379	-77.0 ± 7.8
MKS 21B	Nov 18	Traverse 5	3007	-76.2 ± 7.7
NEP22-26	Nov 22	Traverse 5	2579	-75.4 ± 7.7

Sample ID	Season	Traverse	Elevation	$\Delta G \pm 1\sigma$
			m	kJ/mol
NEP22-27	Nov 22	Traverse 5	3126	-75.3 ± 7.6
NEP22-28	Nov 22	Traverse 5	2954	-75.3 ± 7.7
MKS-14	Nov 18	Traverse 5	2536	-73.5 ± 7.5
NEP24-020	Sep 24	Traverse 5	2556	-73.5 ± 7.5
NEP24-028	Sep 24	Traverse 5	2782	-73.2 ± 7.4
NEP22-29	Nov 22	Traverse 5	2852	-73.0 ± 7.4
NEP22-23	Nov 22	Traverse 5	2517	-72.9 ± 7.4
MKS-20	Nov 18	Traverse 5	1903	-72.7 ± 7.4
NEP22-39	Nov 22	Traverse 5	2523	-72.6 ± 7.4
NEP24-025	Sep 24	Traverse 5	3127	-72.6 ± 7.4
NEP22-24	Nov 22	Traverse 5	2622	-72.5 ± 7.4
MKS 22B	Nov 18	Traverse 5	3130	-72.4 ± 7.4
NEP22-22	Nov 22	Traverse 5	2758	-72.4 ± 7.4
MKS-22	Nov 18	Traverse 5	3126	-72.2 ± 7.4
NEP22-25	Nov 22	Traverse 5	2562	-71.8 ± 7.3
NEP22-30	Nov 22	Traverse 5	2757	-71.7 ± 7.3
NEP24-022	Sep 24	Traverse 5	2259	-71.3 ± 7.3
NEP22-35	Nov 22	Traverse 5	2068	-71.1 ± 7.3
MKS-17	Nov 18	Traverse 5	2163	-71.0 ± 7.2
MKS 15B	Nov 18	Traverse 5	2000	-70.4 ± 7.2
NEP22-32	Nov 22	Traverse 5	2252	-70.4 ± 7.2
NEP24-023	Sep 24	Traverse 5	2269	-70.4 ± 7.2
NEP24-021	Sep 24	Traverse 5	2243	-70.3 ± 7.2
MKS-18	Nov 18	Traverse 5	2262	-70.2 ± 7.1

Sample ID	Season	Traverse	Elevation	$\Delta G \pm 1\sigma$
			m	kJ/mol
NEP22-33	Nov 22	Traverse 5	2247	-70.2 ± 7.1
MKS 18B	Nov 18	Traverse 5	2265	-70.1 ± 7.1
NEP22-31	Nov 22	Traverse 5	2573	-70.1 ± 7.1
NEP22-34	Nov 22	Traverse 5	2240	-70.1 ± 7.1
MKS-16	Nov 18	Traverse 5	1942	-70.0 ± 7.1
MKS-19	Nov 18	Traverse 5	2164	-69.9 ± 7.2
NEP22-37	Nov 22	Traverse 5	2050	-69.0 ± 7.0
NEP22-36	Nov 22	Traverse 5	1987	-68.1 ± 6.9

## 6.4 Model Sensitivity to Concentration

Residence times in Traverse 1 are explainably the longest in the catchment. The springs here are at the lowest elevation, so the flow paths are presumably the longest. This is consistent with the highest DSi concentration of the catchment, and evidence for secondary precipitation of kaolinite at the lowest elevations (see Figure 5(b)). In Traverse 1, the Fontorbe model predicts a peak of  $\approx 100$  years, while the Maher model has a much higher residence time of  $\approx 300$  years. The discrepancy is likely due to how the models are formulated.

Fontorbe	Maher
$T_f = \frac{(C_h - C_0) \cdot \phi}{(1 - f) \cdot R_n}$	$T_f = \frac{C_{eq} \cdot (C - C_0)}{e^2 R_n (C_{eq} - C)}$

Table 6: Comparison of residence time equations from Fontorbe and Maher.

The difference in the models comes from the underlying assumptions of reaction rate and how it changes towards equilibrium. The Fontorbe assumption that reaction rate remains constant as the reaction progresses is unrealistic, as all weathering reactions are bound to stop at some time. Hence, the Maher model more accurately reflects water in these catchments that is closer to equilibrium. The  $\frac{C_{eq}}{(C_{eq}-C)}$  term in the Maher model gets larger as the concentration approaches equilibrium. As a result of this, the Maher model consistently predicts longer residence times than the Fontorbe Model at higher DSi concentrations, while the opposite is true at lower DSi concentrations. For Traverse 1 the  $\frac{C_{eq}}{(C_{eq}-C)}$  term grows arbitrarily large, hence the strong discrepancy found in Figure 5 (c).

For this study's calculations, the equilibrium concentration is taken to be the highest in the catchment,  $869 \mu\text{M}$  DSi. This concentration corresponds the highest spring concentration found in Traverse 1. Note that in the Maher & Chamberlain (2014) model setup, an equilibrium concentration of  $375 \mu\text{M}$  DSi is chosen from the global river data of Gaillardet

et al. (1999). This is sound for a theoretical model but is not appropriate for this catchment. It is unclear, however, whether choosing the highest DSi concentration in the catchment is appropriate. Clearly as this concentration is approached, the Maher model will predict unrealistic residence times, as shown in Figure 11. The free energy of the system suggests the spring system is far away from equilibrium, so choosing a larger  $C_{eq}$  would produce better agreement with the Fontorbe model at higher DSi concentrations and allow for the calculated free energy. Additionally, Maher (2011) details several ways in which  $C_{eq}$  could change depending on the conditions. For example, increasing pCO<sub>2</sub> would increase the concentration of DSi at equilibrium. Another way to potentially estimate the maximum DSi concentration would be to calculate this at equilibrium by simulating further reaction of the most reacted springs with the appropriate minerals. The only assumption here would be that CO<sub>2</sub> is conserved. However, if the Maher model assumes that all flow paths reach equilibrium, it is appropriate to use a concentration measured within the catchment; otherwise, applying the model would be of little relevance to the overall discussion on weathering controls.

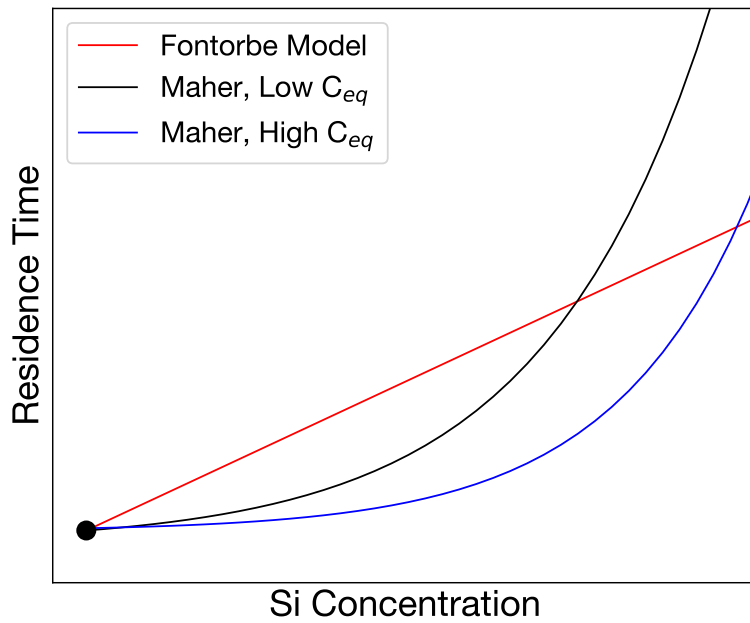


Figure 12: Illustrative sketch of how dissolved silica concentration changes with flow path length for the two models, and different equilibrium concentration for the Maher model. Plotted lines are taken from the model equations 6 and 9.

There is another potential issue related to the dependence of residence time on the concentration of DSi. As is apparent in Figures 5-9 and Table 6, the estimated residence time of both models is directly related to the DSi concentration in the spring water. This is by design, however as expressed in subsection 6.1, low DSi is not necessarily indicative of less reacted groundwater. As a result of this, there is the possibility that the estimated residence times act more as a lower bound. A better approach in a future study could use elemental ratios, for example  $\text{Na}^+/\text{DSi}$  that has a known behaviour as the reaction progresses. Elemental ratios like that would also factor out dilution as a potential influencing factor.

## 6.5 Is the Rate Constant Used Appropriate?

Figure 11 suggests that the system is far away from equilibrium, but the reaction rate constant used in both models for all calculations is one that is only considered feasible when close to equilibrium (Kampman et al., 2009). In systems far from equilibrium, the reaction rate constant has been suggested to be much larger than those used in the models (White & Brantley, 2003). Field rate constants lie between  $10^{-13}$  and  $10^{-17}$  mol m $^{-2}$  s $^{-1}$ , while laboratory rate constants are between  $10^{-11}$  and  $10^{-13}$  mol m $^{-2}$  s $^{-1}$  (White & Brantley, 2003). If the rate constant is increased, the residence times predicted by the models will decrease. This is because the rate of reaction is inversely proportional to the residence time, as seen in the equations in Table 6. Reaction rate constants that are suggested to be far from equilibrium in Kampman et al. (2009) are laboratory-derived rates, and four orders of magnitude higher than those used in this study. Using these rates for the models predicts residence times in the range of 1-10 days. Under the assumption that the rates displayed in Kampman et al. (2009) are accurate for systems far away from equilibrium, the results no longer agree with Atwood (2023). Under these circumstances, then, the Maher and Fontorbe models are less likely to be appropriate for use in discussing weathering controls.

There are, however, counterarguments to this. Firstly, Kampman et al. (2009) investigate river - not spring - water draining a different lithology, under different pH and pCO<sub>2</sub>

conditions than Melamchi. Secondly, the reaction rate constants reported at far from equilibrium free energies are calculated in the laboratory, at different conditions to both this study and Kampman et al. (2009). Field derived reaction rate constants are often found to be lower than those measured in the lab. It is therefore unclear whether the  $k\text{-}\Delta G$  relationship suggested in Kampman et al. (2009) is applicable to Melamchi, or natural catchments in general. In other words, in the absence of field-derived reaction rate constants in far from equilibrium settings, there is little evidence to suggest that the rate constants used in this study, and the models' calculated residence times are incorrect. This therefore suggests that the Maher and Fontorbe model rate constants are appropriate for use in natural catchments.

## 7 Conclusions and Future Work

Elemental concentrations and ratios for different springs in the kinetically-limited Melamchi catchment are reproducible over different field seasons, with dilution in the monsoon season. This suggests that the flow paths coming out of each spring are consistently sampled. Reactive transport models can then be used to estimate residence times in the catchment. Estimated times of order 10-100 years by the Fontorbe and Maher models are consistent with previously obtained gas ages in Melamchi. This study therefore presents a novel approach to predict residence times using the chemistry of spring waters alone. This has implications for predicting weathering controls and resilience to drought in Himalayan catchments. Both models predict similar times at low concentration, suggesting that the system is not close to equilibrium, and free energy calculations agree. The distance of the catchment from equilibrium is inconsistent with the Maher model assumption that all flow paths reach it. The Maher model is likely more appropriate - weathering reactions are ultimately not going to go on indefinitely, so a decreasing reaction rate is a physically realistic assumption. However, the Fontorbe and Maher differ little in Melamchi because the fluids are far from equilibrium at the end of the flow path. Maher's contention that weathering paths always approach equilibrium, and are therefore more sensitive to water flux than temperature, does not hold for Melamchi and by implication other rapidly eroding terrains. Whether this suggests that the greatest control on weathering is temperature is less clear. Calculated free energy is not inconsistent with the Fontorbe model, but this does not mean it is the most appropriate model to use for Melamchi, especially given its reaction rate formulation.

There are caveats to these conclusions. Firstly, depending on the equilibrium concentration chosen for the Maher model, the measured concentrations used and predicted times could be consistent with a far from equilibrium system. The choice of this equilibrium concentration is however linked to the natural system it is found in, so choosing the highest measured concentration in the catchment is considered the most appropriate option. Secondly, just using elemental concentrations has the potential to underestimate residence

times, as a result of secondary precipitation reactions. Lastly, if the system is far from equilibrium, a corresponding rate constant should be used for the model calculations. These rate constants are orders of magnitude larger than those considered close to equilibrium, and so would lead to predicted residence times on the order of days. Nonetheless it is unclear whether these rate constants are appropriate for natural catchments given they were not estimated in a natural setting.

There is significant scope for future work in this area. Elemental ratios are more readily indicative of back-reactions than concentrations alone, and so can be implemented into the models to estimate residence times more accurately. Given model dependence on reaction rate constants, it would be beneficial to quantify a backward reaction rate to add to the forward dissolution rate used in the models. This would allow for secondary precipitation to be accounted for instead of it being a potential source of error. Finally, isotope tracers like  $\delta^2\text{H}$ ,  $\delta^{18}\text{O}$ ,  $\delta^{30}\text{Si}$ ,  $^{87}\text{Sr}/^{86}\text{Sr}$ , and  $\delta^7\text{Li}$  are often proposed for use together in natural catchments to distinguish old and new water because of their ability to identify different aspects of reaction and mixing (Druhan & Benettin, 2023).

## References

- Adhikari, T. R., Baniya, B., Tang, Q., Talchabhadel, R., Gouli, M. R., Budhathoki, B. R., Awasthi, R. P. (2023). "Evaluation of Post Extreme Floods in High Mountain Region: A Case Study of the Melamchi Flood 2021 at the Koshi River Basin in Nepal". In: *Natural Hazards Research* 3.3, pp. 437–446.
- Andermann, C., Longuevergne, L., Bonnet, S., Crave, A., Davy, P., Gloaguen, R. (2012). "Impact of Transient Groundwater Storage on the Discharge of Himalayan Rivers". In: *Nature Geoscience* 5.2, pp. 127–132.
- Atwood, A. C. (2023). "Critical Zone Response to Perturbation: From Mountain Building to Wildfire". PhD thesis. University of Southern California.
- Awolayo, A. N., Tutolo, B. M. (2022). "PyGeoChemCalc: A Python Package for Geochemical Thermodynamic Calculations and Software-Specific Thermodynamic Database Production from Ambient to Deep Earth Conditions". In: *Chemical Geology* 606.
- Baniya, B., Tang, Q., Adhikari, T. R., Zhao, G., Haile, G. G., Sigdel, M., He, L. (2024). "Climate Change Induced Melamchi Extreme Flood and Environment Implication in Central Himalaya of Nepal". In: *Natural Hazards* 120.12, pp. 11009–11029.
- Barry, R. G., Chorley, R. J. (2009). *Atmosphere, Weather and Climate*. 1st. Routledge.
- Berner, R. A. (1978). "Rate Control of Mineral Dissolution under Earth Surface Conditions". In: *American Journal of Science* 278.9, pp. 1235–1252.
- Bethke, C. M. (2011). "Geochemical and Biogeochemical reaction, Second Edition". In: *Cambridge University Press*.
- Bickle, M. J., Tipper, E., Galy, A., Chapman, H., Harris, N. (2015). "On Discrimination between Carbonate and Silicate Inputs to Himalayan Rivers". In: *American Journal of Science* 315.2, pp. 120–166.
- Bookhagen, B., Burbank, D. W. (2010). "Toward a Complete Himalayan Hydrological Budget: Spatiotemporal Distribution of Snowmelt and Rainfall and Their Impact on River Discharge". In: *Journal of Geophysical Research: Earth Surface* 115.F3.

- Bufe, A., Hovius, N., Emberson, R., Rugenstein, J. K. C., Galy, A., Hassenruck-Gudipati, H. J., Chang, J.-M. (2021). "Co-Variation of Silicate, Carbonate and Sulfide Weathering Drives CO<sub>2</sub> Release with Erosion". In: *Nature Geoscience* 14.4, pp. 211–216.
- Chen, C.-M., Hollingsworth, J., Clark, M., Zekkos, D., Chamlagain, D., Bista, S., Siwakoti, A., West, A. J. (2023). "The 2021 Melamchi Flood: A Massive Erosional Cascade in the Himalayan Mountains of Central Nepal". In: *Natural Hazards Research* 3.3, pp. 447–456.
- David, C., Wong, T.-F., Zhu, W., Zhang, J. (1994). "Laboratory Measurement of Compaction-Induced Permeability Change in Porous Rocks: Implications for the Generation and Maintenance of Pore Pressure Excess in the Crust". In: *pure and applied geophysics* 143.1-3, pp. 425–456.
- Dhital, M. R. (2015). *Geology of the Nepal Himalaya*. Regional Geology Reviews. Springer International Publishing.
- Downs, R. T., Hall-Wallace, M. (2003). "The American Mineralogist Crystal Structure Database". In: *American Mineralogist* 88, pp. 247–250.
- Drever, J. I. (1997). *The Geochemistry of Natural Waters: Surface and Groundwater Environments*. 3rd. Upper Saddle River, NJ: Pearson.
- Druhan, J. L., Benettin, P. (2023). "Isotope Ratio – Discharge Relationships of Solutes Derived From Weathering Reactions". In: *American Journal of Science* 323.5.
- Dubacq, B. (2022). "Thermodynamics of Ordering and Mixing in Plagioclase Feldspars: Atomistic Modelling in Favour of Landau Theory". In: *Contributions to Mineralogy and Petrology* 177.10, p. 102.
- Fontorbe, G., De La Rocha, C. L., Chapman, H. J., Bickle, M. J. (2013). "The Silicon Isotopic Composition of the Ganges and Its Tributaries". In: *Earth and Planetary Science Letters* 381, pp. 21–30.
- Gaillardet, J., Dupré, B., Louvat, P., Allègre, C. (1999). "Global Silicate Weathering and CO<sub>2</sub> Consumption Rates Deduced from the Chemistry of Large Rivers". In: *Chemical Geology* 159.1-4, pp. 3–30.
- Garrels, R. M., Mackenzie, F. T. (1967). "Origin of the Chemical Composition of Some Springs and Lakes". In: *Equilibrium Concepts in Natural Water Systems*. Ed. by W. Stumm. Washington DC: American Chemical Society. Chap. 10, pp. 222–242.

- Graf, E. L. S., Sinclair, H. D., Attal, M., Gailleton, B., Adhikari, B. R., Baral, B. R. (2023). *Geomorphological and Hydrological Controls on Sediment Export in Earthquake-Affected Catchments in the Nepal Himalaya*.
- Gran, G. (1952). "Determination of the equivalence point in potentiometric titrations. Part II". In: *Analyst* 77 (920), pp. 661–671.
- Gražulis, S., Merkys, A., Vaitkus, A., Okulič-Kazarinas, M. (2015). "Computing Stoichiometric Molecular Composition from Crystal Structures". In: *Journal of Applied Crystallography* 48.1, pp. 85–91.
- Henry, D. J., Navrotsky, A., Zimmermann, H. D. (1982). "Thermodynamics of plagioclase-melt equilibria in the system albite-anorthite-diopside". In: *Geochimica et Cosmochimica Acta* 46.3, pp. 381–391.
- Jackson, M. D., Blundy, J., Sparks, R. S. J. (2018). "Chemical Differentiation, Cold Storage and Remobilization of Magma in the Earth's Crust". In: *Nature* 564.7736, pp. 405–409.
- Kampman, N., Bickle, M., Becker, J., Assayag, N., Chapman, H. (2009). "Feldspar Dissolution Kinetics and Gibbs Free Energy Dependence in a CO<sub>2</sub>-enriched Groundwater System, Green River, Utah". In: *Earth and Planetary Science Letters* 284.3-4, pp. 473–488.
- Kattel, D. B., Yao, T., Yang, K., Tian, L., Yang, G., Joswiak, D. (2013). "Temperature Lapse Rate in Complex Mountain Terrain on the Southern Slope of the Central Himalayas". In: *Theoretical and Applied Climatology* 113.3-4, pp. 671–682.
- Kelemen, P., Shimizu, N., Salters, V. (1995). "Extraction of Mid-Ocean-Ridge Basalt from the Upwelling Mantle by Focused Flow of Melt in Dunite Channels". In: *Nature* 375, pp. 747–753.
- Knight, A. C., Stevenson, E. I., Bridgestock, L., Jotautas Baronas, J., Knapp, W. J., Adhikari, B. R., Andermann, C., Tipper, E. T. (2024). "The Impact of Adsorption–Desorption Reactions on the Chemistry of Himalayan Rivers and the Quantification of Silicate Weathering Rates". In: *Earth and Planetary Science Letters* 641.
- Kump, L. R., Brantley, S. L., Arthur, M. A. (2000). "Chemical Weathering, Atmospheric CO<sub>2</sub>, and Climate". In: *Annual Review of Earth and Planetary Sciences* 28.1, pp. 611–667.

- Lichtner, P. C. (1988). "The quasi-stationary state approximation to coupled mass transport and fluid-rock interaction in a porous medium". In: *Geochimica et Cosmochimica Acta* 52.1, pp. 143–165.
- Maher, K. (2011). "The Role of Fluid Residence Time and Topographic Scales in Determining Chemical Fluxes from Landscapes". In: *Earth and Planetary Science Letters* 312.1-2, pp. 48–58.
- Maher, K., Chamberlain, C. P. (2014). "Hydrologic Regulation of Chemical Weathering and the Geologic Carbon Cycle". In: *Science* 343.6178, pp. 1502–1504.
- Maher, K., Steefel, C. I., White, A. F., Stonestrom, D. A. (2009). "The Role of Reaction Affinity and Secondary Minerals in Regulating Chemical Weathering Rates at the Santa Cruz Soil Chronosequence, California". In: *Geochimica et Cosmochimica Acta* 73.10, pp. 2804–2831.
- Marques, E. A. G., Barroso, E. V., Menezes Filho, A. P., Vargas, E. d. A. (2010). "Weathering Zones on Metamorphic Rocks from Rio de Janeiro—Physical, Mineralogical and Geomechanical Characterization". In: *Engineering Geology* 111.1–4, pp. 1–18.
- McCallum, J. L., Cook, P. G., Simmons, C. T. (2015). "Limitations of the Use of Environmental Tracers to Infer Groundwater Age". In: *Groundwater* 53.S1, pp. 56–70.
- NASA Space Systems. (2018). *ASTER Global Digital Elevation Model V003*.
- Panthi, J., Dahal, P., Shrestha, M., Aryal, S., Krakauer, N., Pradhanang, S., Lakhankar, T., Jha, A., Sharma, M., Karki, R. (2015). "Spatial and Temporal Variability of Rainfall in the Gandaki River Basin of Nepal Himalaya". In: *Climate* 3.1, pp. 210–226.
- Pedrazas, M. A., Hahm, W. J., Huang, M.-H., Dralle, D., Nelson, M. D., Breunig, R. E., Fauria, K. E., Bryk, A. B., Dietrich, W. E., Rempe, D. M. (2021). "The Relationship Between Topography, Bedrock Weathering, and Water Storage Across a Sequence of Ridges and Valleys". In: *Journal of Geophysical Research: Earth Surface* 126.4.
- Raymo, M. E., Ruddiman, W. F. (1992). "Tectonic Forcing of Late Cenozoic Climate". In: *Nature* 359.6391, pp. 117–122.
- Shand, P., Darbyshire, D. P. F., Goody, D. C. (1999). "The application of Strontium isotopes to catchment studies: The Plynlimon upland catchment of Central Wales". In: *British Geological Survey*.

- Sharma, C. (1997). *A Treatise on Water Resources of Nepal*, p. 493.
- Singh, R. P., Upadhyay, V. K., Das, A. (1987). "Weathering Potential Index for Rocks Based on Density and Porosity Measurements". In: *Proceedings of the Indian Academy of Sciences (Earth and Planetary Sciences)* 96, pp. 239–247.
- Stallard, R. F., Edmond, J. M. (1983). "Geochemistry of the Amazon: 2. The Influence of Geology and Weathering Environment on the Dissolved Load". In: *Journal of Geophysical Research: Oceans* 88.C14, pp. 9671–9688.
- Tipper, E. T., Bickle, M. J., Galy, A., West, A. J., Pomiès, C., Chapman, H. J. (2006). "The Short Term Climatic Sensitivity of Carbonate and Silicate Weathering Fluxes: Insight from Seasonal Variations in River Chemistry". In: *Geochimica et Cosmochimica Acta* 70.11, pp. 2737–2754.
- Vaitkus, A., Merkys, A., Sander, T., Quirós, M., Thiessen, P. A., Bolton, E. E., Gražulis, S. (2023). "A Workflow for Deriving Chemical Entities from Crystallographic Data and Its Application to the Crystallography Open Database". In: *Journal of Cheminformatics* 15.
- West, A., Galy, A., Bickle, M. (2005). "Tectonic and Climatic Controls on Silicate Weathering". In: *Earth and Planetary Science Letters* 235.1-2, pp. 211–228.
- White, A. F., Brantley, S. L. (2003). "The Effect of Time on the Weathering of Silicate Minerals: Why Do Weathering Rates Differ in the Laboratory and Field?" In: *Chemical Geology* 202.3-4, pp. 479–506.
- Wojtowicz, J. A. (2001). "The Thermodynamic Basis of the Saturation Index". In: *Consulting Chemist*.

## Appendix 1: Rain and Hydrothermal Correction Equations

Spring water is corrected for rain input according to the average concentration for the closest rain sample collected in this field season. To remove the contribution of the rain the following formula is used for any element X:

$$[X]_{rain-corrected} = [X]_{river} - (Cl_{river} - Cl_{river}^*) \frac{[X]_{rain}}{[Cl]_{rain}} \quad (16)$$

$$Cl_{river}^* = Cl_{river} - Cl_{rain}; \quad \text{if } Cl_{river} > Cl_{rain} \quad (17)$$

Where  $[Cl]_{river}^*$  is calculated by subtracting the concentration of chloride in the rain from that in the river (Tipper et al, 2006).  $Cl^*$  is taken to be zero if the concentration of chloride in the rain is greater than concentration of river. Evapotranspiration is not considered by this model, and studies which show that it plays a minor role, accounting for less than 10% of the hydrological budget in the Himalayas (Andermann et al (2012); Bookhagen and Burbank, 2010). In those cases where  $Cl^*$  is not zero then, a primary rain correction is simply:

$$[X]_{rain-corrected} = [X]_{river} - [X]_{rain} \quad (18)$$

Once the samples have been corrected for rain input, the remaining  $[Cl]^-$  is assumed to be derived from hydrothermal springs encountered in the flow path. This is likely to be the case in one of the southern traverses (Traverse 2) in Melamchi which display high chloride concentrations even after the cyclic correction. Hence, the sample with the highest  $[Cl]^-$  is used to correct:

$$[X]_{hydrothermal-corrected} = [X]_{rain-corrected} - \frac{[X]}{[Cl]_{highest-Cl}} * [Cl]_{rain-corrected} \quad (19)$$

This ensures that all chloride in the corrected sample is removed. The correction uses ionic ratios from the most concentrated water source, which acts as a proxy for the sediment imparting its signature. In this way, the correction does not affect samples which do not have high Cl (and hence do not have a large hydrothermal contribution), but does decrease the concentration of ions for those that do.

## Appendix 2: Derivation of Reactive Transport Models

### Fontorbe et al. (2013) Model Derivation

---

This model investigates silicon isotopic composition in the Ganges River, assuming constant reaction rates along flow paths. The model is initially built to predict DSi concentrations, but in this study it is adapted to calculate residence times.

The first-order differential equation governing transport and reaction is given as:

To simplify, we introduce non-dimensional variables:

$$\phi \frac{\partial C}{\partial t} = -\omega \phi \frac{\partial C}{\partial z} + R_n(1-f) \quad (20)$$

$$C' = \frac{C}{C_o}, \quad z' = \frac{z}{h}, \quad t' = \frac{t\omega}{h} \quad (21)$$

Rewriting Equation 21 using these new variables:

$$\frac{\partial C'}{\partial t'} = -\frac{\partial C'}{\partial z'} + N_D(1-f) \quad (22)$$

The Damköhler number ( $N_D$ ) describes the relative importance of kinetic vs transport-controlled settings (Bethke, 2011):

$$N_D = \frac{R_n h}{\phi C_o \omega} \quad (23)$$

Assuming a quasi-stationary state ( $\partial C'/\partial t' = 0$ ),

$$C' = 1 + z' N_D (1-f) \quad (24)$$

we get:

At the end of the flow path ( $z = h, z' = 1$ ), this simplifies to:

$$N_D = \frac{C' - 1}{1 - f} \quad (25)$$

The residence time of water along the flow path is:

$$T_f = \frac{h}{\omega} \quad (26)$$

At the end of the flow path:

$$\frac{R_n h}{\phi C_o \omega} = \frac{C' - 1}{1 - f} \quad (27)$$

$$\frac{R_n T_f}{\phi C_o} = \frac{C' - 1}{1 - f} \quad (28)$$

Solving for residence time  $T_f$  and reaction rate  $R_n$ :

$$T_f = \frac{(C - C_o)\phi}{(1 - f)R_n} \quad (29)$$

$C$  is the concentration at the end of the flow path, which is taken to be equal to the concentration of each spring, assuming each spring represents a unique flow path. Note that given these units, the calculation gives time in  $10^{-3}$ s. This is converted to years for practical use.

<b>Fontorbe</b>			
<b>Parameter</b>	<b>Definition</b>	<b>Units</b>	<b>Formula (Value)</b>
$\phi$	Porosity	-	0.1*
$\omega$	Fluid velocity	m/s	Variable
$h$	Length of flow path	m	Variable
$C$	Concentration end of flow path	$\mu\text{mol/L}$	Variable
$C_0$	Initial concentration	$\mu\text{mol/L}$	Rain Input
$f$	Fraction reprecipitated	-	0.5*
$N_D$	Damkohler Number	-	$N_D = \frac{R_n h}{\phi C_0 \omega}$
$T_f$	Residence time	s	$T_f = \frac{h}{\omega \phi}$
$R_n$	Reaction rate	$\text{mol}/\text{m}^3/\text{s}$	$\rho \cdot 10^6 \cdot k \cdot S \cdot X$
$k$	Dissolution rate constant	$\text{mol}/\text{m}^2/\text{s}$	$10^{-15}*^*$
$S$	Specific surface area	$\text{m}^2/\text{g}$	0.1*
$\rho$	Plagioclase density	$\text{g}/\text{cm}^3$	2.7*
$X$	Volume fraction of mineral in rock	$\text{g}_{\text{min}}/\text{g}_{\text{rock}}$	0.2*

Table A1: Key parameters and definitions for the Fontorbe model. \* - Values used for calculation.

## Maher (2011) Model Derivation

---

This model describes a reaction-based approach to solute transport, following Maher & Chamberlain (2014). Maher (2011) suggests a dissolution rate law which decreases linearly to zero at equilibrium. The first-order differential equation governing transport and reaction is:

$$\frac{dC}{dt} = -\frac{q}{\theta} \frac{dC}{dz} + \sum_i \mu_i R_{d,i} \left(1 - \left(\frac{C}{C_{eq}}\right)^{n_i}\right)^{m_i} - \sum_i \mu_i R_{p,i} \left(1 - \left(\frac{C}{C_{eq}}\right)^{n_i}\right)^{m_i} \quad (30)$$

Where  $C$  is the concentration in  $\mu\text{mol/L}$ ,  $q$  is the flow rate in  $\text{m/s}$ ,  $\theta$  is the volumetric water content in  $\text{m}^3$ ,  $z$  is the position along the flow path in  $\text{m}$ ,  $\mu$  is the stoichiometric coefficient dependent on the reacting minerals,  $R$  is the rate of reaction for dissolution and precipitation respectively in  $\text{mol/L/s}$ ,  $C_{eq}$  is the equilibrium concentration in  $\mu\text{mol/L}$ , and  $n$  and  $m$  are non-linear parameters (Maher, 2011). Defining the net reaction rate for a set of packets  $i$ :

$$R_n = \sum_i \mu_i R_{d,i} - \sum_i \mu_i R_{p,i} \quad (31)$$

Maher and Chamberlain describe that the reaction rate decreases linearly with approach to equilibrium.

$$\frac{dC}{dt} = R_n \left(1 - \frac{C}{C_{eq}}\right) \quad (32)$$

Solving for  $C$ , following Maher & Chamberlain (2014):

$$C = C_0 \exp\left(-\frac{R_n \theta h}{q C_{eq}}\right) + C_{eq} \left(1 - \exp\left(-\frac{R_n \theta h}{q C_{eq}}\right)\right) \quad (33)$$

The residence time  $T_f$  is defined as:

$$T_f = \frac{h\phi}{q} \quad (34)$$

Thus, at residence time  $T_f$ :

$$c(T_f) = c_0 \exp\left(-\frac{R_n T_f}{c_{eq}}\right) + c_{eq} \left(1 - \exp\left(-\frac{R_n T_f}{c_{eq}}\right)\right) \quad (35)$$

Following Maher & Chamberlain (2014), this can be rewritten as:

$$C = \frac{C_0}{1 + \tau D_w / q} + C_{eq} \frac{\tau D_w / q}{1 + \tau D_w / q} \quad (36)$$

Where:

$$\tau = e^2; \quad D_w = \frac{h\theta R_n}{C_{eq}} \quad (37)$$

Rewriting the equation:

$$C = \frac{C_0 + C_{eq} \cdot T_f (e^2 \cdot R_n / C_{eq})}{1 + T_f (e^2 \cdot R_n / C_{eq})} \quad (38)$$

Solving for residence time  $T_f$ :

$$T_f = \frac{C_{eq} \cdot (C - C_0)}{e^2 R_n (C_{eq} - C)} \quad (39)$$

Note that given these units, the calculation gives time in  $10^{-3}$  s. This is converted to years for practical use. Also note the  $e^2$  term is used because the Maher model considers all paths as if they approach equilibrium.

<b>Maher</b>			
<b>Parameter</b>	<b>Definition</b>	<b>Units</b>	<b>Formula (Value)</b>
$\phi$	Porosity	-	0.1*
$h$	Length of flow path	m	Variable
$q$	Flow rate	m/s	Variable
$C_{eq}$	Equilibrium concentration	$\mu\text{mol/L}$	Max Catchment
$C_0$	Initial concentration	$\mu\text{mol/L}$	Rain Input
$R_n$	Net reaction rate	$\text{mol/L/s}$	$\rho \cdot 10^6 \cdot k \cdot S \cdot X$
$\rho$	Plagioclase density	$\text{g/cm}^3$	2.7*
$k$	Dissolution rate constant	$\text{mol/m}^2/\text{s}$	$10^{-15}*^*$
$S$	Specific surface area	$\text{m}^2/\text{g}$	0.1*
$X$	Volume fraction of mineral in rock	$g_{min}/g_{rock}$	0.2*
$\tau$	Scaling factor	-	$\tau = e^2$
$D_w$	Damkohler Coefficient	$\text{m}^2/\text{s}$	$D_w = \frac{L\phi R_n}{C_{eq}}$
$T_f$	Residence time	s	$T_f = \frac{h\phi}{q}$

Table A2: Key parameters and definitions for the Maher model. \* - Values used for calculation.